JOURNAL OF PETROLOGY

Journal of Petrology, 2016, Vol. 56, No. 12, 2491–2514
doi: 10.1093/petrology/egv076
Original Article

OXFORD

Using Platinum Group Elements to Identify Sulfide Saturation in a Porphyry Cu System: the El Abra Porphyry Cu Deposit, Northern Chile

Helen A. Cocker[1]*, Dianne L. Valente[2], Jung-Woo Park[1,3] and Ian H. Campbell[1]

[1]Research School of Earth Sciences, Australian National University, Canberra, ACT 0200, Australia; [2]BHP Billiton Iron Ore, PO Box 655, Newman, WA 6753, Australia and [3]School of Earth and Environmental Sciences & Research Institute of Oceanography, Seoul National University, Seoul 151-747, South Korea

*Corresponding author. E-mail: helen.cocker@anu.edu.au

Received September 30, 2014; Accepted November 27, 2015

ABSTRACT

Geochronological and geochemical studies, including platinum group element (PGE) analyses, were undertaken on samples from the El Abra–Pajonal igneous complex, northern Chile, to investigate the magmatic evolution of the suite. Special attention was paid to identifying the onset of sulfide saturation and to documenting how it influenced the geochemistry of the chalcophile elements and the formation of the El Abra porphyry Cu deposit. The PGE have extreme sulfide melt–silicate melt partition coefficients, making them sensitive indicators of the timing of sulfide saturation in an evolving magmatic system. In arc-related intermediate to felsic magmatic systems, which have the potential to produce porphyry deposits, the timing and extent of sulfide saturation relative to ore-fluid saturation may control the capacity of these systems to produce economic mineralization and, if they do, whether the deposits are Cu-only or Cu–Au. This study incorporates the first comprehensive analysis of PGE in a felsic magmatic suite associated with an economic porphyry system. The suite comprises a series of quartz monzodiorite to granite intrusions with U–Pb zircon ages between 43 and 35 Ma. Their petrography and major element chemistry, including increasing Sr/Y ratios and rare earth element patterns, suggest that crystal fractionation and crustal assimilation were the key magmatic processes governing the evolution of the El Abra–Pajonal suite. Plagioclase fractionation dominated the oldest intrusions, and their associated granites and aplites. Following the injection of a more primitive, wetter, mafic magma at 41–40 Ma, plagioclase fractionation became suppressed and amphibole became the dominant fractionating phase, leading to the formation of the El Abra porphyry intrusion and Cu deposit. Abundances of Pt and Pd in felsic rocks from the El Abra–Pajonal intrusive complex drop rapidly in samples with MgO values below 2·5 wt %, following sulfide saturation of the magmas, which occurred slightly before ore-fluid saturation and formation of the Cu deposit. Modeling suggests that the amount of sulfide formed was very small, enough to strip the PGE and Au from the magma but not Cu, because of the lower partition coefficient of Cu relative to the precious metals, which explains why the mineralization at El Abra is a Cu-only porphyry deposit, rather than a Cu–Au deposit.

Key words: El Abra; platinum group elements; porphyry copper deposits; sulfide saturation; U–Pb dating

INTRODUCTION

Porphyry systems

The majority of the world's Cu production comes from porphyry Cu deposits, making an understanding of their genesis a critical factor in Cu exploration. Porphyry deposits are typically large-tonnage, low- to medium-grade deposits. They are frequently associated with other intrusion-related hydrothermal mineralization systems such as skarn and epithermal deposits (Mudd *et al.*, 2013). Characteristics of porphyry deposits, including associated magmatic and hydrothermal processes, have been summarized in numerous recent review papers including those by Seedorff *et al.* (2005), Sillitoe (2010), Audétat & Simon (2012) and Kouzmanov & Pokrovski (2012), and in references therein.

Porphyry Cu systems typically develop in association with magmatic arcs above subduction zones. The ascending magmas form intermediate to felsic intrusions of 'calc-alkaline to alkaline' composition that are relatively oxidized and hydrous. The deposits are associated with shallow intrusive porphyry stocks, which are interpreted to originate from deeper parent magma bodies (Dilles, 1987; Seedorff *et al.*, 2005, 2008; Sillitoe, 2010). The shallow ore-associated intrusions exsolve magmatic fluids, which, along with circulating meteoric water, hydrothermally alter the host-rock and deposit ore minerals. There are many different aspects of porphyry formation that influence porphyry mineralization. These include the composition of the magma, oxidation state, timing of magmatic processes (including sulfide and ore-fluid saturation), depth of emplacement, and geodynamic setting (Candela, 1997; Cooke *et al.*, 2005; Seedorff *et al.*, 2005; Sillitoe, 2010). The interplay among these factors controls the quantity and type of porphyry mineralization that will form.

El Abra, northern Chile (Fig. 1), is a classic example of a porphyry copper deposit with excellent exposures of a complete suite of weakly altered plutonic rocks that are directly associated with the ore body. It is therefore an ideal natural laboratory in which to examine the magmatic processes that lead to the formation of porphyry Cu deposits, by addressing two key questions: How did the El Abra–Pajonal magmatic suite evolve though time? What influenced and controlled the porphyry mineralization? This study focuses on understanding the connection between the magmatic processes involved in the evolution of the El Abra–Pajonal suite intrusions and the El Abra porphyry Cu mineralization being mined today. Therefore, the nature of the deposit itself, in terms of mineralization, alteration, and veining style for example, has not been studied, but rather we have focused on the temporal and chemical development of the intrusions directly associated with the mineralization, using petrographic, geochemical, and geochronological analytical techniques. Special emphasis has been placed on the role of the timing of sulfide saturation relative to ore-fluid saturation, using the platinum group elements (PGE) to pinpoint the onset of sulfide saturation.

Fig. 1. Location map showing El Abra deposit and some of the other major porphyry Cu deposits in the region.

Sulfide saturation

The PGE have been successfully used to identify sulfide saturation in mafic systems (e.g. Keays & Lightfoot, 2007) but analytical difficulties have limited their application in felsic systems. Recent advances in the inductively coupled plasma mass spectrometry (ICP-MS)–NiS fire assay–isotope dilution method (Park *et al.*, 2012) now make it possible to measure the PGE at the 1–20 ppt level, so that they can now be analyzed in rocks with very low abundances, including felsic suites. As a consequence, PGE geochemistry can be now used to identify the onset of sulfide saturation in evolving felsic magmas, which can potentially be used to distinguish between Cu- and/or Au-bearing and barren felsic systems. The initial hypothesis we set out to test is that if a fractionating magmatic system becomes sulfide saturated before it becomes ore-fluid saturated most of the Cu and Au will be trapped within sulfides in a deep parent magma chamber and be unavailable to enter a hydrothermal fluid, which emanates from one of the shallow daughter intrusions, the El Abra porphyry. Alternatively, if ore-fluid saturation occurs before sulfide saturation most of the Cu and Au will be available to partition into the magmatic hydrothermal fluid,

which could lead to the formation of an economic Cu and/or Au deposit.

The PGE are preferred to Au and Cu for identifying sulfide saturation in evolving silicate melts for two reasons. First, the partition coefficients for Pt and Pd into an immiscible sulfide melt are approximately two orders of magnitude higher than those for Au and Cu (Mungall & Brenan, 2014). As a consequence, Pd and Pt are much more sensitive indicators of sulfide fractionation. Second, the original Au and Cu content of the rocks can be overprinted by secondary Cu and/or Au mineralization, making it impossible to obtain the primary concentration of these elements in samples. Although the ore-forming fluid can carry Pd, the amount is trivial compared with Cu and Au. For example, the Au/Pd ratio of the primitive mantle (McDonough & Sun, 1995) and basaltic magmas, prior to sulfide saturation (Park *et al.*, 2013*a*, 2015), is typically 0·25–0·8 but it averages over 90 for a wide range of Pd-rich porphyries analyzed by Tarkian & Stribrny (1999). Bearing in mind that the Pd content of many of the analyzed samples was below their detection limit of 8 ppb, the high Au/Pd ratio of porphyry ore implies that Au is at least 100 times more soluble than Pd in the ore-forming fluid.

Sulfide saturation in the evolution of porphyry systems has been discussed in the recent literature but pertains to either theoretical suppositions or analysis of silicate and sulfide melt inclusions and typically entails later breakdown of the sulfides to release the chalcophile elements into the ore fluid for deposit formation (Keith *et al.*, 1997; Halter *et al.*, 2002, 2005; Richards, 2009; Audétat & Simon, 2012; Wilkinson, 2013). In this study the whole-rock abundances of Pt and Pd are used to identify the occurrence and timing of sulfide saturation, relative to ore-fluid saturation, in an evolving magmatic system that produced a porphyry Cu deposit. The identification of sulfide saturation in arc-related magmatic systems using PGE abundances has been previously demonstrated and discussed by Park *et al.* (2013*a*, 2013*b*, 2015) but the method has not been applied to porphyry mineralization. This study presents the first use of PGE to identify sulfide saturation in a felsic ore system associated with a significant porphyry Cu deposit. The El Abra deposit and associated El Abra–Pajonal intrusive complex makes an ideal study area because it is a well-exposed suite that exhibits a range of chemical compositions (quartz monzodiorite to granite), leading up to the formation of a porphyry Cu deposit. A secondary aim of this study is to determine why El Abra is a Cu-only system and to determine its place in a continuum of Cu ± Au (± PGE-enriched) systems [for a discussion of PGE enrichment in porphyry systems see Tarkian & Stribrny (1999) and Economou-Eliopoulos (2005)]. It does not aim to address all of the different types of porphyry systems, such as Cu ± Au ± Mo, but instead attempts to understand how sulfide saturation in a crustal magmatic system controls Cu ± Au porphyry mineralization.

GEOLOGICAL SETTING

El Abra is an economic porphyry Cu-only deposit in northern Chile associated with the El Abra–Pajonal complex, a suite of intermediate to felsic intrusive rocks (Fig. 2; Ambrus, 1977; Dilles *et al.*, 1997). The initial Cu-oxide reserve for the El Abra deposit at the commencement of mining in 1995 was 798 million tons at 0·54 wt % Cu (Gerwe, 2005) whereas the Cu-sulfide ore reserve was 452 million tons at 0·64 wt % Cu (Graichen *et al.*, 1995). The deposit occurs within a deep-seated, NW-trending shear zone that is linked to the West Fissure Fault Zone (Graichen *et al.*, 1995; Barrett, 2004; Gerwe, 2005), a major fault that is part of the Domeyko Fault system and is associated with many other porphyry Cu deposits in the region, including, from north to south, Collahuasi District, Chuquicamata, La Escondida and El Salvador (Fig. 1; Ambrus, 1977; Reutter *et al.*, 1996; Cornejo *et al.*, 1997; Garza *et al.*, 2001; Ossandon *et al.*, 2001; Richards *et al.*, 2001; Masterman *et al.*, 2005; Urqueta *et al.*, 2009).

Copper ± molybdenum mineralization is centered on an El Abra porphyry stock that crosscuts the El Abra–Pajonal suite of intrusions, which range in composition from alkali feldspar granite to quartz monzodiorite (Ambrus, 1977; Graichen *et al.*, 1995; Barrett, 2004; Gerwe, 2005). These intrusions delineate a southwards younging trend from the Cerro de Pajonal Mountain. The active mining area lies within a potassic alteration zone that extends up to 1600 m radially from the host El Abra porphyry stock (Graichen *et al.*, 1995; Barrett, 2004; Gerwe, 2005). The deposit is characterized by high-grade Cu (±Mo and Zn), low-S mineralization, with Cu grades decreasing radially from the core of the deposit (Ambrus, 1977; Graichen *et al.*, 1995; Barrett, 2004; Gerwe, 2005). High-grade Cu mineralization is associated with K-feldspar-dominated potassic alteration (Ambrus, 1977); however, the highest Cu grades occur along NW-trending fissures and veins within the potassic alteration zone (Graichen *et al.*, 1995; Barrett, 2004; Gerwe, 2005). The lowest Cu grades occur within the propylitic alteration zone (Ambrus, 1977; Graichen *et al.*, 1995; Barrett, 2004; Gerwe, 2005). Hypogene mineralization is observed to extend to depths >900 m (Graichen *et al.*, 1995; Barrett, 2004) and is generally characterized by chalcopyrite, either intergrown with bornite (Ambrus, 1977) or rimmed by bornite and chalcocite (Graichen *et al.*, 1995; Barrett, 2004). Molybdenite is a minor accessory phase that occurs peripheral to the Cu-rich core of the deposit (Ambrus, 1977; Graichen *et al.*, 1995; Barrett, 2004), such that molybdenite grades increase with decreasing Cu grades (Ambrus, 1977). Galena and sphalerite mineralization are found in the youngest veins within the El Abra deposit (Ambrus, 1977; Gerwe, 2005). Supergene mineralization is coincident with an oxide cap that overlies the hypogene mineralization and this cap extends to a maximum depth of 600 m (Graichen *et al.*, 1995; Barrett, 2004). Chrysocolla is the dominant oxide mineral mined; however,

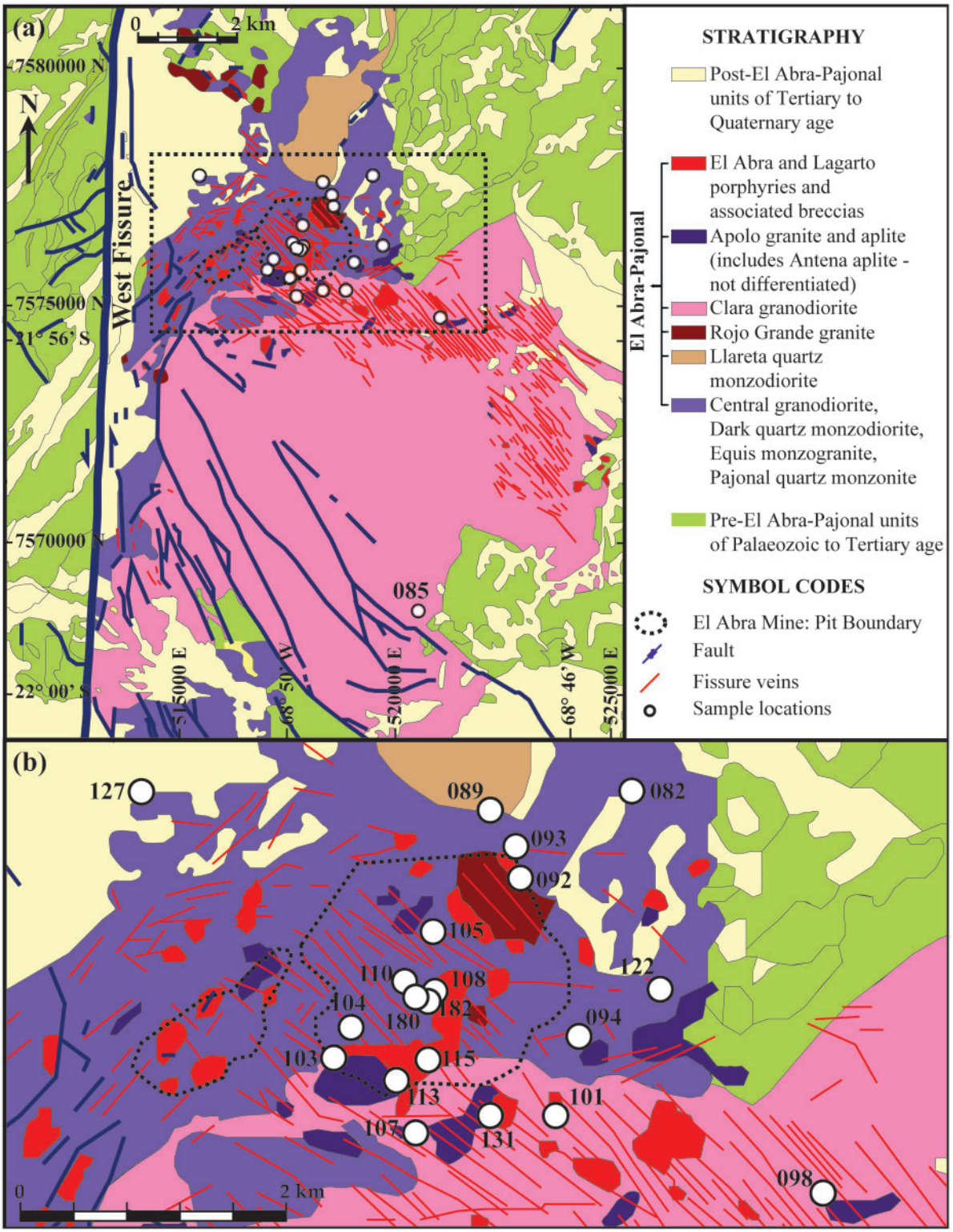

Fig. 2. (a) Geological map of the El Abra region showing location of the samples used in this study. The area within the dashed rectangle is shown enlarged in (b). Grid references for each sample are included in Table 2. Those samples labeled with numbers (with the ANU07 prefix omitted) refer to samples that were chosen for PGE and Re analysis. Simplified geological map modified from Tomlinson *et al.* (1995) and Barrett (1997). Post-El Abra–Pajonal units of Tertiary to Quaternary age include the Carcote ignimbrite and Tertiary and Quaternary gravels. Pre-El Abra–Pajonal units of Palaeozoic to Tertiary age include the Icanche Formation, Saturno fanglomerate, Cerro Colorado Complex, Tolar Formation, and Collahuasi Formation. Projection UTM 19K, datum South America Provisional 1956.

turquoise, tenorite, antlerite, brochantite, Cu-wad and Cu-rich clays are also observed within the oxide zone (Graichen *et al.*, 1995; Barrett, 2004). Native Cu and cuprite are commonly found along the irregular and gradational oxide (supergene)–hypogene contact (Graichen *et al.*, 1995; Barrett, 2004).

SAMPLES AND METHODS

Samples were collected from all units of the El Abra–Pajonal intrusive complex including the El Abra porphyry. Fresh to weakly altered samples were chosen where possible to avoid mineralization, although some weakly altered samples have small amounts of disseminated hydrothermal sulfide.

U–Pb zircon dating, combined with zircon trace element analyses, was carried out on 26 samples previously analyzed for whole-rock chemistry. The dating technique used in this study is similar to that of Harris *et al.* (2004) and Campbell *et al.* (2006). Zircons were separated from 2 kg samples by a combination of standard crushing, magnetic separation and heavy liquid techniques. Epoxy resin mounts with zircons from up to four samples of unknown age and three standards [Temora-2 (Black *et al.*, 2004); NIST610 (Kane, 1998); 521-Los Picos (Ballard, 2001)] were set and polished. Cathodoluminescence (CL) images and optical photography were used to assist with selection of ablation sites. Laser ablation (LA) was conducted using a pulsed ArF LambdaPhysik LPX 120i UV Excimer Laser at 5 Hz with an operating voltage varying between 20 and 23 kV and a spot size of 32 μm. Particular attention was paid to the selection of rims versus cores as inherited cores are common in zircons from the nearby Chuquicamata region (Zentilli *et al.*, 1994; Ballard, 2001). Ablated material was transported from the laser sample cell via a mixture of *c.* 70% Ar, 29% He and $<1\%$ H_2 gas to an Agilent 7500s ICP-MS system for analysis. Counts for ^{29}Si, ^{91}Zr, ^{31}P, ^{206}Pb, ^{207}Pb, ^{208}Pb, ^{232}Th, ^{235}U and ^{238}U were collected in time-resolved mode. Additional isotopes ^{49}Ti, ^{89}Y, ^{139}La, ^{140}Ce, ^{144}Sm, ^{153}Eu, ^{163}Dy, ^{175}Lu and ^{177}Hf were also collected. As the carrier gas contains ^{204}Hg, it impossible to measure ^{204}Pb owing to the direct isobaric interference. Following the procedure described by Campbell *et al.* (2006) the raw data were corrected for instrumental mass bias drift, isotopic fractionation, depth-dependent elemental fractionation and common Pb, using the glass NIST610 and zircons from the Temora-2 standard. The zircon standard 521-Los Picos was processed in the same manner as unknown samples and used for quality control. The corrections were applied on an ablation-time (depth) basis. The Temora-2 standard was also used to correct for depth-dependent, inter-element fractionation of $^{207}Pb/^{206}Pb$, $^{208}Pb/^{232}Th$, $^{206}Pb/^{238}U$ and $^{207}Pb/^{235}U$, by using the known ratios from Black *et al.* (2004). ^{235}U was calculated from ^{238}U assuming $^{235}U = {}^{238}U/137{\cdot}88$, except in extremely U-rich samples where mass ^{235}U was measured directly. The average $^{206}Pb/^{238}U$ correction factor applied to each mass scan for unknown zircons was based on the ratio between the measured Temora-2 $^{206}Pb/^{238}U$ ratio value (for multiple Temora-2 measurements over the course of an analytical session) to the Black *et al.* (2004) $^{206}Pb/^{238}U$ ratio value. Applying this method to correct for depth-dependent fractionation assumes that variation in the fractionation factor with ablation depth is similar in the unknown zircon and Temora-2 standard. The glass standard, NIST610, was used to determine concentrations for all elements following a procedure similar to that described for the isotope ratios. Two methods, the ^{207}Pb and ^{208}Pb correction methods, were used to correct for common Pb [see Campbell *et al.* (2006) for details]. The ^{208}Pb method to correct for common Pb is preferred to the ^{207}Pb method and has been used in this study. Both methods give dates that, with rare exceptions, agree within analytical error. Zircons were considered to be discordant if their ^{207}Pb-corrected or ^{208}Pb-corrected $^{206}Pb/^{238}U$ age divided by their ^{207}Pb-corrected or ^{208}Pb-corrected $^{207}Pb/^{235}U$ age, was greater than 1 ± 0.1, including errors. Discordant zircons were rejected from the age calculation. The quoted 2 SE for the U–Pb zircon age for a single zircon is the error derived from two components: the analytical uncertainty of the zircon measurement, and the uncertainty in the measurement of the standards. The standard deviation for Temora-2 was used to measure the uncertainty of the standards for each analytical session (Supplementary Data Table A1; supplementary data for this paper are available at http://www.petrology.oxfordjournals.org). The data were processed using the ISOPLOT software of Ludwig (2012) to generate weighted average $^{238}U/^{206}Pb$ ages.

Whole-rock major element concentrations of 47 El Abra–Pajonal suite samples were measured by X-ray fluorescence (XRF) on fused-glass disks using a Philips PW2400 XRF spectrometer at the University of Otago. Whole-rock trace element concentrations were analyzed at the Australian National University by laser ablation (LA)-ICP-MS on the same glass disks that were used for the XRF analyses. The system used was a pulsed ArF LambdaPhysik LPX 120i UV excimer laser connected to an Agilent 7500s ICP-MS system operated at 5 Hz with a voltage varying between 20 and 23 kV, with a pit diameter of 70 μm and ablation depth of *c.* 20 μm in 40 s. NIST612 was used as the primary standard and BCR-2 was used to monitor quality control.

Whole-rock PGE and Re abundances in 21 selected samples were determined by the modified NiS fire assay isotope dilution method described by Park *et al.* (2012). Only intrusions directly related to the magmatic evolution of the El Abra porphyry (mineralizing event) were included for PGE analysis. The Antena aplite, Rojo Grande granite and Apolo granite were excluded because their geochemistry precludes them being part of the suite that evolved to form the ore-associated El Abra porphyry. Duplicate analyses were also run with a Te co-precipitation step, following a method based on that of Jackson *et al.* (1990) and Savard *et al.* (2010). The Te and Sn solutions were, however, diluted to 1% of the concentrations described by Savard *et al.* (2010) to reduce the blank in the PGE

solutions to acceptable levels. A single-collector Agilent 7700 ICP-MS system at the Australian National University was used to analyze the final solutions. A detailed description of the methods used and all of the data for the whole-rock samples analyzed in this study, procedural blanks and reference material samples are given in the Supplementary Data (Tables A2 and A3). The method limits of detection, taken as three standard deviations of the procedural blanks, were 0·5 ppt for Ir, 1·3 ppt for Ru, 1·4 ppt for Rh, 19·7 ppt for Pt, 9·5 ppt for Pd, and 8·2 ppt for Re. Total uncertainties in the data primarily result from uncertainty in the blank subtraction and ICP-MS counting statistics. The reference material TDB-1 (CCRMP-CANMET diabase) was used to assess the accuracy and precision of the measurements. Our analyses of the PGE and Re abundances in TDB-1 and error measurements are reported in Table A3 in the Supplementary Data and are consistent with the previously reported values of Plessen & Erzinger (1998), Peucker-Ehrenbrink *et al.* (2003), Meisel & Moser (2004) and Savard *et al.* (2010).

Ce^{4+}/Ce^{3+} ratios in zircon were calculated using the whole-rock and zircon Ce concentrations determined by LA-ICP-MS of XRF fused disks and zircons, respectively. The zircon Ce^{4+}/Ce^{3+} ratio values are based on the preferential partitioning of Ce^{4+} into the zircon structure over Ce^{3+}. Calculation of the ratios follows the method of Ballard *et al.* (2002) using the following equation:

$$(Ce^{4+}/Ce^{3+})_{zircon} = \frac{Ce_{melt} - \frac{Ce_{zircon}}{D^{zircon/melt}_{Ce^{3+}}}}{\frac{Ce_{zircon}}{D^{zircon/melt}_{Ce^{4+}}} - Ce_{melt}}$$

where the whole-rock (Ce_{melt}) concentrations of Ce and Ce in zircon (Ce_{zircon}) are from this study and the partition coefficients for Ce^{4+} and Ce^{3+} are estimated from plots of distribution coefficients of tetravalent and trivalent cations (Ballard *et al.*, 2002).

PETROGRAPHY

Descriptions of each of the intrusive units of the El Abra–Pajonal suite are given below in order of youngest to oldest, based on their U–Pb zircon ages in conjunction with field and drill core observations. A comparison of this revised nomenclature with other studies of the El Abra–Pajonal complex is provided in Supplementary Data Table A4. The intrusions of the El Abra–Pajonal suite consist of varying amounts of amphibole, plagioclase, orthoclase, quartz, and biotite, together with minor amounts of Ti-magnetite and accessory apatite, zircon, titanite, and rutile. The samples studied are fresh to weakly altered with small amounts (0 to *c.* 5%) of disseminated hydrothermal sulfide mineralization, predominantly pyrite and chalcopyrite.

Lagarto porphyry

The Lagarto porphyry is dacitic, with the dominant phenocryst mineralogy being biotite (pseudomorphic after amphibole) and plagioclase. Plagioclase is notable for its lack of oscillatory zoning; instead crystals feature large cores with thin rims. An inclusion-rich layer defines the contact between rims and cores. Orthoclase and quartz are also present as phenocrysts, with quartz commonly strongly resorbed. Phenocrysts are subhedral to euhedral and vary in size from 0·5 to 8 mm (average size is 1 mm). Trace amphibole (partly replaced by biotite) is also observed. The groundmass varies from glassy to aphanitic (<0·01–0·1 mm), and mineralogically includes quartz, plagioclase, orthoclase, and Ti-magnetite. Apatite and zircon are the accessory phases. Small miarolitic cavities are present in thin-section.

El Abra porphyry

The main mineralization event at El Abra is associated with the El Abra porphyry. Dykes and stocks of this porphyry crosscut all the main intrusive units in the El Abra–Pajonal suite, excluding the Lagarto porphyry and Pajonal quartz monzonite. The El Abra porphyry is a moderately porphyritic dacite with phenocrysts ranging in size from 0·5 to 2 mm and groundmass microlites from 0·01 to 0·1 mm. Thin-section microscopy shows that the phenocryst mineralogy is dominated by plagioclase and amphibole, with later-forming biotite, orthoclase and quartz. The groundmass mineralogy consists of Ti-magnetite, quartz, orthoclase, plagioclase and accessory phases including apatite, zircon, and orange- and lemon-colored titanite. Plagioclase crystals occasionally show oscillatory zoning and some crystals do not have distinct cores and rims. Amphibole and titanite are common inclusions in plagioclase. Amphibole phenocrysts feature abundant inclusions including quartz, apatite, chalcopyrite, titanite and magnetite. Smaller-sized amphibole phenocrysts are often zoned, with the euhedral cores and rims resorbed.

Apolo granite

The Apolo granite (and aplite) is a leucocratic granite containing a maximum of 5% mafic minerals (biotite and magnetite) with a coarse (1–5 mm) holocrystalline texture. The mineralogy includes anhedral to euhedral quartz, orthoclase and minor plagioclase, biotite and Ti-magnetite, with accessory minerals including rutile, apatite, and zircon. The Apolo granitic and aplitic stocks crosscut the Clara granodiorite.

Clara granodiorite

The Clara granodiorite is a coarse-grained, holocrystalline rock (grain size varies from 0·2 to 2 mm, with an average size of 1 mm). Mineral shapes range from subhedral to euhedral and the paragenesis is amphibole (with rare quartz or plagioclase inclusions), weakly oscillatory-zoned plagioclase, quartz, Ti-magnetite, biotite, microcline and orthoclase. Accessory minerals include orange- and lemon-colored titanite, apatite (often very coarse grained, up to 0·1 mm in size) and zircon. Accessory chalcopyrite occurs as inclusions in amphibole and plagioclase. Previously, the Clara

granodiorite has been mapped and subdivided into two sub-members, the Mafic Clara granodiorite and Leucocratic Clara granodiorite (Ambrus, 1977; Tomlinson *et al.*, 1995). No crosscutting igneous relationships or chilled margins were observed in the field between the two sub-members of the Clara granodiorite and there is no difference in the major element chemistry of these two sub-units. Furthermore, the dating work completed for this study showed that all samples from the Clara granodiorite have the same age within analytical error. These observations support the view of Dilles *et al.* (1997) that the Clara granodiorite represents one intrusive event.

Rojo Grande granite

The Rojo Grande granite is distinguished from the Apolo granite by containing on average 5 wt % less SiO_2 than the Apolo granite and having a greater abundance of mafic minerals (10–15%). The Rojo Grande granite has a coarse (1–5 mm) holocrystalline texture; its principal minerals are anhedral to euhedral biotite (up to 10%), quartz, orthoclase and plagioclase, with trace amounts of amphibole (magnesio-hornblende and actinolite) and Ti-magnetite. Accessory minerals include orange- and lemon-colored titanite, apatite, zircon, and trace rutile.

Llareta quartz monzodiorite

The Llareta quartz monzodiorite is an equigranular, medium- to coarse-grained (0·5–2 mm) unit composed of amphibole, biotite, Ti-magnetite, orthoclase, plagioclase and quartz. Apatite, zircon, lemon-colored titanite and trace rutile are the accessory minerals.

Dark quartz monzodiorite

The Dark quartz monzodiorite is distinctive and is the most mafic unit in the El Abra–Pajonal suite. It is equigranular in texture and fine grained (0·1–0·5 mm). The mineralogy includes subhedral to euhedral amphibole, biotite, Ti-magnetite, orthoclase, microcline, oscillatory-zoned plagioclase, and quartz. Accessory minerals are apatite, zircon, chalcopyrite (as inclusions in amphibole) and lemon-colored titanite.

Central granodiorite

The Central granodiorite is one of the major rock units in the active mining area. Texturally it is equigranular and medium to coarse grained (0·5–2 mm). The mineralogy includes amphibole, biotite, Ti-magnetite, orthoclase, plagioclase and quartz. The accessory minerals are apatite, zircon, chalcopyrite (as inclusions in amphibole), orange-colored titanite and rutile.

Equis monzogranite

The Equis monzogranite is a major rock unit in the active mining area. Texturally it is equigranular and medium to coarse grained (0·5–2 mm). The mineralogy includes amphibole, biotite, Ti-magnetite, orthoclase, plagioclase and quartz. Apatite, zircon, orange-colored titanite, chalcopyrite (as inclusions in amphibole) and rutile are present as accessory minerals.

Pajonal quartz monzonite

Outcrop of the Pajonal quartz monzonite is confined to north of the pit area, on the Cerro de Pajonal Mountain. Texturally it is equigranular and medium to coarse grained (0·5–2 mm); its mineralogy includes orthoclase, plagioclase, quartz, amphibole, biotite, Ti-magnetite and trace amounts of clinopyroxene. Accessory minerals include apatite, zircon and lemon-colored titanite, with trace amounts of ilmenite.

Aplites

Mafic, fine-grained (<0·01–1 mm), equigranular to weakly porphyritic aplites are abundant in the northern and eastern sections of the El Abra–Pajonal complex including the pit. Chemically, these aplites have *c.* 3 wt % less SiO_2 than the Apolo aplites and *c.* 10 wt % more SiO_2 than the Pajonal quartz monzonite and Central granodiorite. Therefore on this basis they have been distinguished as a new, separate intrusive unit named the Antena aplite. The type area for this new unit is a small stock on top of the Cerro de Pajonal Mountain (Tomlinson *et al.*, 1995). Orthoclase, plagioclase, quartz, biotite and trace amounts of amphibole are the major minerals present. The accessory minerals are apatite, zircon, lemon-colored titanite, Ti-magnetite and rutile. The Antena aplite is not related to the Antena granodiorite, a member of the Los Picos–Fortuna complex (Campbell *et al.*, 2006).

RESULTS

U–Pb zircon ages

The ^{208}Pb-corrected ^{206}Pb–^{238}U emplacement ages for the dated samples from the El Abra–Pajonal igneous complex are listed in Table 1. The order of emplacement of the intrusions based on their U–Pb ages is as follows: Pajonal quartz monzonite, 43·21 ± 0·21 Ma; Antena aplite, 42·83 ± 0·22 Ma; Equis monzogranite, 41·73 ± 0·19 Ma; Dark quartz monzodiorite, 40·83 ± 0·33 Central granodiorite, 40·64 ± 0·24 Ma; Llareta quartz monzodiorite, 40·10 ± 0·40 Ma; Rojo Grande granite, 39·21 ± 0·2 Ma; Clara granodiorite, 37·83 ± 0·19 Ma; Apolo granite, 37·55 ± 0·26 Ma; El Abra porphyry, 36·89 ± 0·30 Ma; Lagarto porphyry, 35·53 ± 0·47 Ma. Uncertainties are quoted at the 95% confidence level. A number of the intrusions were emplaced at the same time within the analytical uncertainty of the LA-ICP-MS U–Pb zircon dating method; in these cases, field and drill-core relationships were used to resolve the intrusion order. However, the order of emplacement of the intrusions at *c.* 40–41 Ma (Central granodiorite, Dark quartz monzodiorite, and Llareta quartz monzodiorite) remains unclear. Figure 3 shows weighted average U–Pb ages for single samples, as well as the weighted

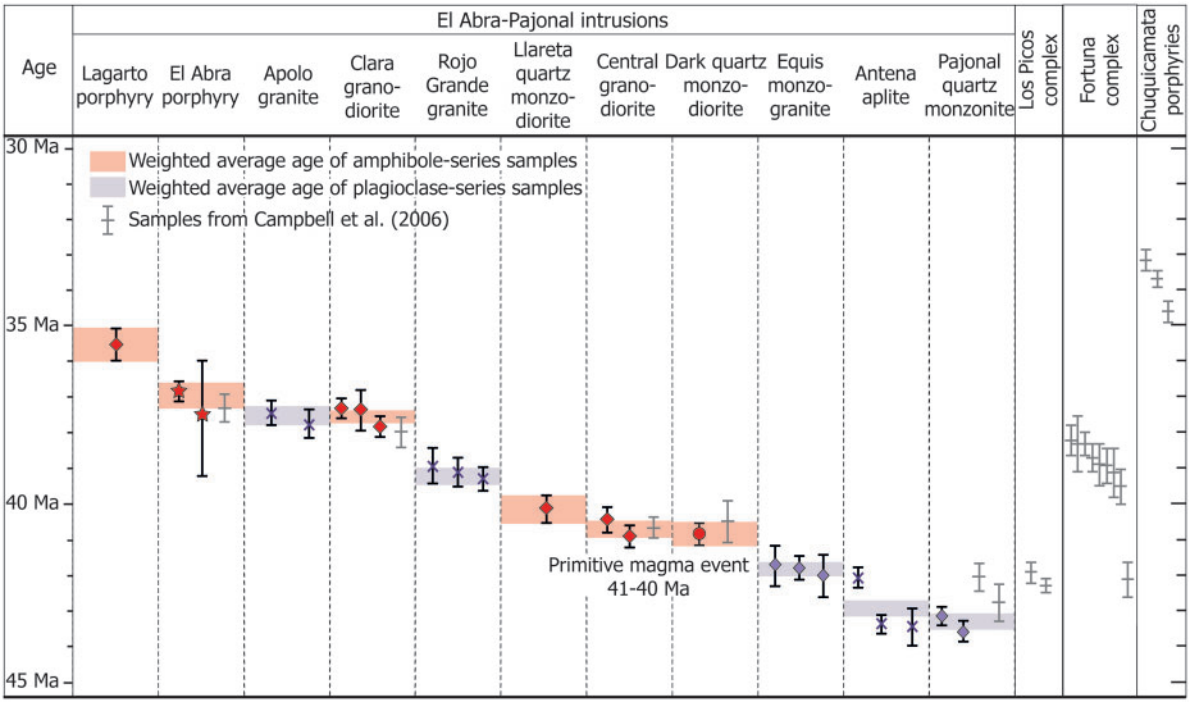

Fig. 3. $^{206}Pb/^{238}U$ zircon ages for the El Abra–Pajonal suite samples. Shaded areas represent average ages for each intrusion analysed in this study. Errors shown are 2 SD of the weighted average. Also shown are U–Pb zircon ages of El Abra–Pajonal, Los Picos, Fortuna, and Chuquicamata samples from Campbell *et al.* (2006) for comparison; these are not included in the weighted average age.

average from the total zircon population for each intrusion.

Whole-rock major and trace element geochemistry

Whole-rock major and trace element data for representative samples of each intrusive unit are reported in Table 2. Figures 4 and 5 show the variation of selected whole-rock major and trace elements. The intrusions have been divided into two series: a Plagioclase series and an Amphibole series. There is a general trend of decreasing TiO_2, Al_2O_3, Fe_2O_3, MgO, CaO and P_2O_5 with increasing SiO_2 (Table 2; Fig. 4a and b). Fe_2O_3 decreases with decreasing MgO, as is typical of 'calc-alkaline' arc suites (Fig. 4d). Al_2O_3, Na_2O and K_2O show two distinct trends related to the different Plagioclase and Amphibole fractionation series (Fig. 4a, c and e). The Amphibole series shows little variation in Al_2O_3 with SiO_2 or K_2O with MgO, and only a gradual increase in Na_2O with decreasing MgO. In contrast, the Plagioclase series samples show decreasing Al_2O_3 with increasing SiO_2, and decreasing Na_2O and increasing K_2O with decreasing MgO. The MgO and Ni contents of the most primitive Amphibole series samples are higher than those of the most primitive Plagioclase series samples and the most fractionated Amphibole series samples have lower SiO_2 (Fig. 4b). Many trace elements (e.g. Y, La, Dy, Cr, Cu, Ba) show considerable scatter and are weakly correlated or show no correlation with SiO_2; this may also be partly due to weak alteration of the samples. TiO_2 and Ni decrease with decreasing MgO (Figs 4f and 5a); however, Fig. 4f shows two decreasing TiO_2 trends. Samples from the Plagioclase series that are older than 41 Ma (Pajonal quartz monzonite, Antena aplite, Equis monzogranite) have higher TiO_2 concentrations than those from the Amphibole series at similar MgO concentrations. In contrast, Cu plotted against MgO shows no trend (Fig. 5b). A plot of Sr/Y against Eu/Eu* (Fig. 5c), where $Eu/Eu^* = Eu_N/\sqrt{(Sm_N Gd_N)}$, shows further differences between the Amphibole and Plagioclase series. Samples from the Plagioclase series show a steady decrease in Sr/Y with decreasing Eu/Eu* whereas those from the Amphibole series plot in two clusters with a distinct gap between them. Amphibole series samples with the highest Sr/Y also have the highest Eu/Eu* but the decrease in Eu/Eu* is appreciably less than for the Plagioclase series.

Chondrite-normalized (Palme & O'Neill, 2014) rare earth element (REE) plots are shown in Fig. 6 and show distinct differences between the Amphibole and Plagioclase series. Members of the Amphibole series, which include the Dark quartz monzodiorite, Central granodiorite, Llareta quartz monzodiorite, Clara granodiorite, and the El Abra and Lagarto porphyries, are plotted in Fig. 6a. They are characterized by Eu anomalies that are small or absent and that tend to decrease with increased fractionation. The heavy REE (HREE) also decrease with fractionation whereas the light REE (LREE) change little or increase slightly. The most evolved samples (e.g. the El Abra porphyry) have

Table 1: U-Pb zircon age results for samples from the El Abra-Pajonal igneous complex showing ^{208}Pb-corrected ^{206}Pb/^{238}U emplacement ages (Ma).

Sample	Intrusive unit	^{208}Pb corrected, ^{206}Pb/^{238}U emplacement age (Ma)	2σ[1]	MSWD	*n*
ANU07-118	*Lagarto porphyry*	35·53	0·47	1·03	10
ANU07-094	El Abra porphyry	36·80	0·32	0·72	22
ANU07-107	El Abra porphyry	37·50	1·80	1·90	4
El Abra porphyry average age:		36·89	0·30	0·93	26
ANU07-081	Apolo granite	37·45	0·33	0·88	26
ANU07-119	Apolo granite	37·72	0·43	1·04	17
Apolo granite average age:		37·55	0·26	0·94	43
ANU07-085	Clara granodiorite	37·82	0·28	0·99	31
ANU07-098	Clara granodiorite	37·31	0·29	1·07	27
ANU07-099	Clara granodiorite	37·32	0·60	0·16	6
Clara granodiorite average age:		37·55	0·19	1·04	64
ANU07-095	Rojo Grande granite	39·31	0·37	1·30	38
ANU07-112	Rojo Grande granite	38·93	0·52	1·30	24
ANU07-102	Rojo Grande granite	39·08	0·46	1·40	28
Rojo Grande granite average age:		39·21	0·22	1·00	85
ANU07-089	*Llareta quartz monzodiorite*	40·10	0·40	1·05	19
ANU07-103	Central granodiorite	40·88	0·32	0·88	44
ANU07-113	Central granodiorite	40·37	0·38	1·20	36
Central granodiorite average age:		40·64	0·24	1·08	80
ANU07-101	*Dark quartz monzodiorite*	40·83	0·33	0·99	28
ANU07-105	Equis monzogranite	42·01	0·65	2·20	23
ANU07-110	Equis monzogranite	41·73	0·36	1·40	38
ANU07-127	Equis monzogranite	41·63	0·67	1·01	72
Equis monzogranite average age:		41·73	0·19	1·13	133
ANU07-087	Antena aplite	43·33	0·26	0·75	32
ANU07-091	Antena aplite	43·42	0·58	1·12	7
ANU07-096	Antena aplite	42·03	0·31	1·11	40
Antena aplite average age:		42·83	0·22	1·30	76
ANU07-082	Pajonal quartz monzonite	43·50	0·32	1·14	28
ANU07-122	Pajonal quartz monzonite	42·97	0·26	0·91	34
Pajonal quartz monzonite average age:		43·21	0·21	1·12	62

[1]All uncertainties are standard error at 95% confidence limits.

unusual spoon-shaped or concave-up HREE patterns. Samples from the Plagioclase series, which are older than 41 Ma, are plotted in Fig. 6b. They include the Pajonal quartz monzonite, Antena aplite and Equis monzogranite and are characterized by pronounced Eu anomalies, which increase with fractionation, as do all of the REE, such that the patterns remain subparallel as the concentrations of the REE increase. The patterns for the HREE are again slightly spoon shaped. Figure 6c shows the patterns for the Rojo Grande and Apolo granites. The Rojo Grande granite is geochemically similar to the suite plotted in Fig. 6b but is distinctly younger. The Apolo granite is also younger than the intrusions plotted in Fig. 6b and has strong Eu anomalies that can be positive or negative; the concentrations of the REE are lower than in the other suites. This combination suggests that cumulate processes dominate the geochemistry of the Apolo granite.

Whole-rock PGE and Re results

Whole-rock Pt and Pd abundances are reported for 21 El Abra–Pajonal samples in Table 3; all PGE and Re values are blank subtracted. The other analyzed PGE were below or close to the limit of detection and are therefore not considered further. Re abundances were measurable in 20 samples and range from <8·2 ppt to 46·7 ppb, but show no clear trend.

Abundances of Pd and Pt are plotted versus whole-rock MgO contents for each of the El Abra–Pajonal suite samples in Fig. 7a and b, and are compared with those for samples from Pual Ridge and Niuatihi–Motutahi in Fig. 7c and d. As in previous figures the samples are divided into the Amphibole and Plagioclase series. The plot of Pd versus MgO shows no clear trend for the Amphibole series samples with MgO above 2·5 wt % (Fig. 7a), but Pd falls rapidly once the MgO content falls below this value. The abundance of Pt decreases continuously with decreasing MgO but the rate of decrease becomes more rapid once MgO drops below 2·5 wt % (Fig. 7b). Samples from the ore-bearing El Abra porphyry have both low MgO values and low Pt and Pd abundances, with the exception of the sample with the lowest MgO content, which has an anomalously high Pt abundance. The Plagioclase series samples all have MgO <2·5 wt %. Both Pd and Pt decrease with decreasing MgO for these samples; Pd decreases at a similar rate in the Amphibole series samples with <2·5 wt % MgO; Pt overall decreases more gradually than in the Amphibole series samples below 2·5 wt % MgO. The El Abra–Pajonal suite samples run in duplicate are shown

Table 2: Whole-rock major (as wt % oxides) and trace element (in ppm) concentrations for drill hole and hand samples from the El Abra–Pajonal igneous complex analysed in this study

Sample:	ANU 07-116	ANU 07-115	ANU 07-094	ANU 07-107	ANU 07-081	ANU 07-098	ANU 07-085	ANU 07-095
Intrusive unit:	Lagarto porphyry	El Abra porphyry	El Abra porphyry	El Abra porphyry	Apolo granite	Clara granodiorite	Clara granodiorite	Rojo Grande granite
Drill hole:	LAG04-17	98-30		EA220				
Depth interval (m):	206·55–211·60	596·13–599·98		97·30–97·85				
Easting:	524503	517774	519018	517584	517020	520784	520420	518951
Northing:	7573503	7576309	7576551	7575736	7575880	7575364	7569653	7576493
wt %								
SiO_2	63·88	67·77	65·83	65·46	76·84	63·92	63·94	70·60
TiO_2	0·49	0·32	0·41	0·47	0·13	0·49	0·51	0·34
Al_2O_3	17·31	16·38	17·06	16·91	12·76	17·27	17·13	14·73
$Fe_2O_3^t$	3·31	2·57	3·24	3·33	0·60	3·78	3·97	2·41
MnO	0·17	0·03	0·04	0·05	0·00	0·06	0·06	0·02
MgO	1·55	1·05	1·14	1·54	0·15	1·46	1·72	0·97
CaO	2·75	2·87	2·92	3·00	0·88	4·37	4·35	1·93
Na_2O	4·64	4·56	4·75	4·40	3·00	4·68	4·46	3·38
K_2O	2·57	2·89	2·54	2·67	5·20	2·35	2·57	4·26
P_2O_5	0·23	0·15	0·18	0·20	0·01	0·21	0·21	0·10
LOI	1·78	0·71	1·08	1·02	0·50	0·40	0·50	0·61
Total	98·68	99·30	99·19	99·05	100·07	98·99	99·42	99·35
ppm								
Sc	7·62	5·31	6·37	7·38	2·32	8·03	8·78	6·84
V	157	125	138	154	97·1	156	163	131
Cr	43·3	53	32	66	59·2	50·6	49·8	70·4
Co	7·7	4·57	4·93	6·69	0·75	8·69	8·61	7·2
Ni	6·66	5·75	6·77	8·91	5·26	8·33	8·76	7·8
Cu	3149	292	217	1688	273	89·1	12·5	370
Zn	60·1	27·6	71·6	27·9	18·6	104	43·7	72·5
Ga	17·5	17·4	18	17·5	14·7	18·1	17·8	15·6
Ge	7·03	7·38	7·04	6·97	6·17	6·81	7·01	7·49
As	1·47	1·27	1·55	1·25	1·42	5·04	0·95	3·27
Rb	48·2	50	42·2	77·5	169	53·3	59·1	172
Sr	704	608	708	640	148	727	685	294
Y	8·36	7·07	8·52	8·57	2·16	9·27	9·35	18
Zr	122	130	119	119	51·8	125	138	161
Nb	7·2	6·66	7·19	7·27	7	6·65	6·61	14·6
Mo	49·6	1·11	1·28	30·2	6·38	1·69	2·44	1·81
Ag	0·75	0·19	0·19	0·54	0·28	0·16	0·13	0·18
Sn	1·45	0·68	0·94	1·39	0·59	0·96	0·98	1·17
Cs	4·49	1·12	0·57	4·98	3·58	2·17	1·7	8·64
Ba	704	774	760	658	367	701	719	555
La	21·8	20·7	21·6	24·4	7·08	22·9	22·1	27·5
Ce	41·3	38·1	40	42·8	9·6	42·2	40·4	50·5
Pr	4·81	4·19	4·55	4·63	0·84	4·82	4·66	5·63
Nd	19·3	16	17·6	17·6	2·71	19·1	18·3	20·9
Sm	3·42	2·6	2·96	2·94	0·45	3·29	3·14	3·78
Eu	0·93	0·71	0·8	0·84	0·22	0·88	0·89	0·71
Gd	2·36	1·97	2·11	2·15	0·38	2·41	2·39	3·23
Dy	1·65	1·35	1·53	1·66	0·32	1·81	1·85	3·03
Ho	0·3	0·24	0·29	0·3	0·08	0·33	0·34	0·62
Er	0·83	0·69	0·8	0·86	0·22	0·93	0·91	1·85
Tm	0·14	0·1	0·12	0·12	0·04	0·14	0·15	0·29
Yb	0·9	0·78	0·83	0·9	0·36	0·92	0·97	2·25
Lu	0·12	0·12	0·12	0·14	0·08	0·15	0·15	0·34
Hf	3·29	3·75	3·34	3·4	2·48	3·57	3·97	5·44
Ta	0·52	0·61	0·57	0·61	0·67	0·53	0·57	1·89
Pb	16·4	7·96	21·4	8·81	11·4	8·4	8·64	7·44
Th	4·87	6·34	5·83	7·61	14·1	6·9	6·87	36·1
U	1·82	1·56	1·87	3·09	4·01	1·91	2·29	12·7

(continued)

with filled symbols. In some cases the duplicates lie within plotting error and only a single point is plotted. Where there is a distinct difference between duplicates a connecting line has been drawn between them. Samples with MgO >2·5 wt % (Amphibole series) show greater scatter in Pt than Pd, which shows no significant variation between duplicates, whereas for samples with MgO <2·5 wt % both Pt and Pd show similar scatter.

When plotted against age, there is a distinct spike in several elements, for example MgO and Pd abundances at 40–41 Ma (Fig. 8a and c), which correspond to the emplacement of the Dark quartz monzodiorite and

Table 2: Continued

Sample:	ANU 07-089	ANU 07-093	ANU 07-104	ANU 07-103	ANU 07-113	ANU 07-101	ANU 07-108
Intrusive unit:	Llareta quartz monzodiorite	Llareta quartz monzodiorite	Central granodiorite	Central granodiorite	Central granodiorite	Dark quartz monzo-diorite	Dark quartz monzo-diorite
Drill hole:			98-32	98-011	EAS01-19	EA02-87	EA261
Depth interval (m):			500·80–501·30	117·90–118·46	395·10–395·64	91·44–91·63	41·00–41·23
Easting:	518313	518423	517176	517031	517574	518750	517754
Northing:	7578084	7577656	7576506	7576293	7576175	7575849	7576741
wt %							
SiO_2	63·90	63·60	64·28	59·31	63·38	56·81	53·96
TiO_2	0·57	0·56	0·59	0·79	0·64	0·77	0·83
Al_2O_3	16·55	16·53	16·38	17·49	16·11	17·65	17·26
$Fe_2O_3^t$	4·32	4·63	3·84	6·58	4·12	7·25	8·36
MnO	0·08	0·08	0·04	0·08	0·03	0·09	0·10
MgO	1·80	1·90	2·07	2·90	2·71	3·50	4·18
CaO	4·13	4·26	3·53	5·33	3·40	6·31	6·81
Na_2O	4·27	4·07	3·63	3·79	3·38	3·40	3·37
K_2O	2·90	3·10	3·31	2·18	2·84	2·20	2·32
P_2O_5	0·19	0·19	0·18	0·25	0·22	0·30	0·21
LOI	0·65	0·35	1·38	0·75	1·85	0·92	1·61
Total	99·36	99·27	99·23	99·45	98·68	99·20	99·01
ppm							
Sc	10·4	11·2	11·1	16·5	13·1	18·3	26·9
V	171	173	178	229	191	232	299
Cr	44·6	54·3	60	55·2	62·8	46·3	47
Co	10·1	10·4	13·5	18·5	10·7	18·6	22·3
Ni	10	10·6	14·2	20·2	12·8	16·2	16·5
Cu	30·4	13·6	1445	49·7	2135	293	1168
Zn	84·4	53·4	43·2	60·7	34	53·7	105
Ga	17·7	17·5	16·7	18·6	16·9	18·5	17·1
Ge	7·04	6·7	7·26	6·51	6·54	6·81	7·02
As	5·71	2·62	1·43	2·1	2·18	5·53	2·25
Rb	94·9	113	101	76·4	97·7	72·7	85·8
Sr	545	543	551	615	444	710	672
Y	14·1	13·9	13·7	19·5	17·6	19·8	21·6
Zr	165	150	147	181	191	142	139
Nb	8·45	8·71	8·63	9·93	10·2	9·79	6·05
Mo	1·39	1·84	447	4·85	13·5	11·4	3·91
Ag	0·16	0·13	0·65	0·11	0·87	0·16	0·29
Sn	1·13	1·05	1·03	1·28	1·39	1·53	2·02
Cs	4·47	5·91	4·87	4·11	4·69	3·38	4·72
Ba	644	667	703	562	653	480	535
La	23·3	21	21·8	26·7	26·8	26·8	21·2
Ce	45·9	40·6	43·5	52·3	53·6	53	43
Pr	5·44	4·88	5·09	6·18	6·29	6·34	5·3
Nd	22	19·8	20·5	25·6	25	26·1	22·5
Sm	4·16	3·86	3·83	4·95	4·76	5·02	4·66
Eu	0·89	0·87	0·9	1·21	1·01	1·25	1·12
Gd	3·31	3·16	3·13	4·16	3·84	4·34	4·34
Dy	2·7	2·65	2·66	3·64	3·32	3·71	4·05
Ho	0·51	0·51	0·49	0·7	0·63	0·71	0·78
Er	1·44	1·37	1·39	2·02	1·77	2	2·34
Tm	0·21	0·21	0·21	0·29	0·27	0·3	0·34
Yb	1·47	1·45	1·44	2·02	1·8	2·04	2·34
Lu	0·22	0·22	0·21	0·3	0·26	0·31	0·36
Hf	4·67	4·43	4·2	4·98	5·2	4·24	3·93
Ta	0·76	0·72	0·7	0·79	0·75	0·82	0·45
Pb	21·2	14·7	6·13	6·04	6·39	5·28	5·19
Th	13·6	15·6	13	14·9	14·8	17·7	11·7
U	3·82	4·24	3·66	4·09	4·02	5·01	3·31

(continued)

Central granodiorite intrusions. The Dark quartz monzodiorite is the most mafic of the El Abra–Pajonal suite intrusions. Samples from the Amphibole series show an increase in Sr/Y ratios versus decreasing U–Pb age, whereas those from the Plagioclase series show no clear trend (Fig. 8b).

Cerium ratios

Zircon Ce^{4+}/Ce^{3+} ratios were measured to monitor variations in the relative oxidation state of the melt and the median, upper and lower quartiles of the Ce^{4+}/Ce^{3+} ratios are plotted against the average age for each of the El Abra–Pajonal intrusions used for PGE

Table 2: Continued

Sample:	ANU07-105	ANU07-127	ANU07-110	ANU07-091	ANU07-082	ANU07-092	ANU07-122
Intrusive unit:	Equis monzogranite	Equis monzogranite	Equis monzogranite	Antena aplite	Pajonal quartz monzonite	Pajonal quartz monzonite	Pajonal quartz monzonite
Drill hole:	EA140		EA265				
Depth interval (m):	62·12–62·52		53·17–55·57				
Easting:	517827	515415	517548	518815	519413	518509	519587
Northing:	7577174	7578224	7576739	7578060	7578213	7577554	7576834
wt %							
SiO_2	64·94	66·46	64·58	73·01	64·83	62·73	62·19
TiO_2	0·42	0·61	0·83	0·31	0·78	0·59	0·85
Al_2O_3	16·73	15·04	15·58	13·44	15·38	16·88	15·93
$Fe_2O_3^t$	4·16	4·21	3·90	1·95	4·86	4·73	5·48
MnO	0·02	0·06	0·02	0·02	0·04	0·07	0·09
MgO	1·29	1·39	2·09	0·52	1·77	2·06	2·35
CaO	2·81	3·07	1·70	1·20	3·30	4·55	4·38
Na_2O	3·97	3·31	3·99	3·19	3·54	4·01	3·60
K_2O	2·81	4·66	3·74	5·30	4·29	3·18	3·79
P_2O_5	0·13	0·15	0·13	0·05	0·18	0·21	0·20
LOI	1·32	0·31	1·26	0·43	0·36	0·43	0·48
Total	98·60	99·27	97·82	99·42	99·33	99·44	99·34
ppm							
Sc	7·96	11·7	15·5	6·27	14·2	11·5	16·6
V	146	168	201	112	189	185	207
Cr	39·6	51·7	54·2	58·8	53·6	45·5	75·9
Co	7·13	9·33	9·92	2·75	10·3	11	14·8
Ni	6	8·66	13	5·73	12·5	11·6	15·6
Cu	3692	54·6	5493	31·4	42·5	58·1	72
Zn	37·1	46·4	55	51	30·7	48	44·3
Ga	16·5	16·5	16·2	15·1	16·9	17·7	16·9
Ge	6·96	6·9	6·82	6·64	7·02	6·53	7·09
As	1·57	1·45	1·76	3·83	5·83	3·8	1·09
Rb	99·9	220	120	325	215	114	169
Sr	543	299	298	157	305	583	380
Y	18·5	27·2	23	31·2	26·9	13·9	25
Zr	173	386	331	242	371	172	320
Nb	8·78	14	12·8	16·4	14·9	8·59	13
Mo	7·1	1·8	5·11	3·79	2·81	1·07	1·68
Ag	0·28	0·13	1·48	0·18	0·14	0·15	0·16
Sn	1·32	1·57	1·74	2·21	2·34	1·09	1·97
Cs	2·97	9·83	4·52	15·2	12	6·1	8·66
Ba	927	705	591	449	582	765	663
La	20·5	34·5	27·2	48·7	37·4	19·5	31·9
Ce	42·1	71·5	54·6	98·9	75·9	39	64·6
Pr	4·99	8·41	6·34	10·9	8·93	4·7	7·67
Nd	20	32·9	25·2	38·8	34·6	19·3	30·7
Sm	3·76	6·35	4·77	6·92	6·49	3·78	5·97
Eu	0·97	0·95	0·99	0·6	0·99	0·93	1·08
Gd	3·32	5·4	4·25	5·48	5·46	3·11	5·17
Dy	3·01	4·81	4·14	5·24	4·97	2·62	4·68
Ho	0·62	0·95	0·82	1·07	0·97	0·48	0·9
Er	1·85	2·78	2·43	3·15	2·81	1·36	2·6
Tm	0·28	0·41	0·36	0·5	0·42	0·21	0·38
Yb	2·02	2·84	2·51	3·6	2·87	1·41	2·61
Lu	0·31	0·43	0·38	0·52	0·42	0·22	0·38
Hf	4·84	10·4	8·95	8·22	10·1	4·76	8·39
Ta	0·84	1·23	1·01	2·13	1·28	0·7	0·98
Pb	11·7	12·3	10	13·4	11·3	12·8	10·4
Th	16·4	38·5	25·4	86·7	42	13·6	32
U	5·63	6·99	7·39	12·5	10·2	3·83	7·84

LOI, loss on ignition.

analysis in Fig. 8d. There is a general trend in the median ratio values of increasing Ce^{4+}/Ce^{3+} with increasing magmatic fractionation for samples from the Amphibole series, which implies that the suite became more oxidized with time. This is important because the oxidation state of the melt has a controlling influence on the solubility of sulfur in the melt as will be discussed further below. Samples from the Plagioclase series show little or no increase in Ce^{4+}/Ce^{3+} with time (Fig. 8d).

DISCUSSION

Zircon age correlations

The majority of the average ages for the intrusive units of the El Abra–Pajonal igneous complex from this study

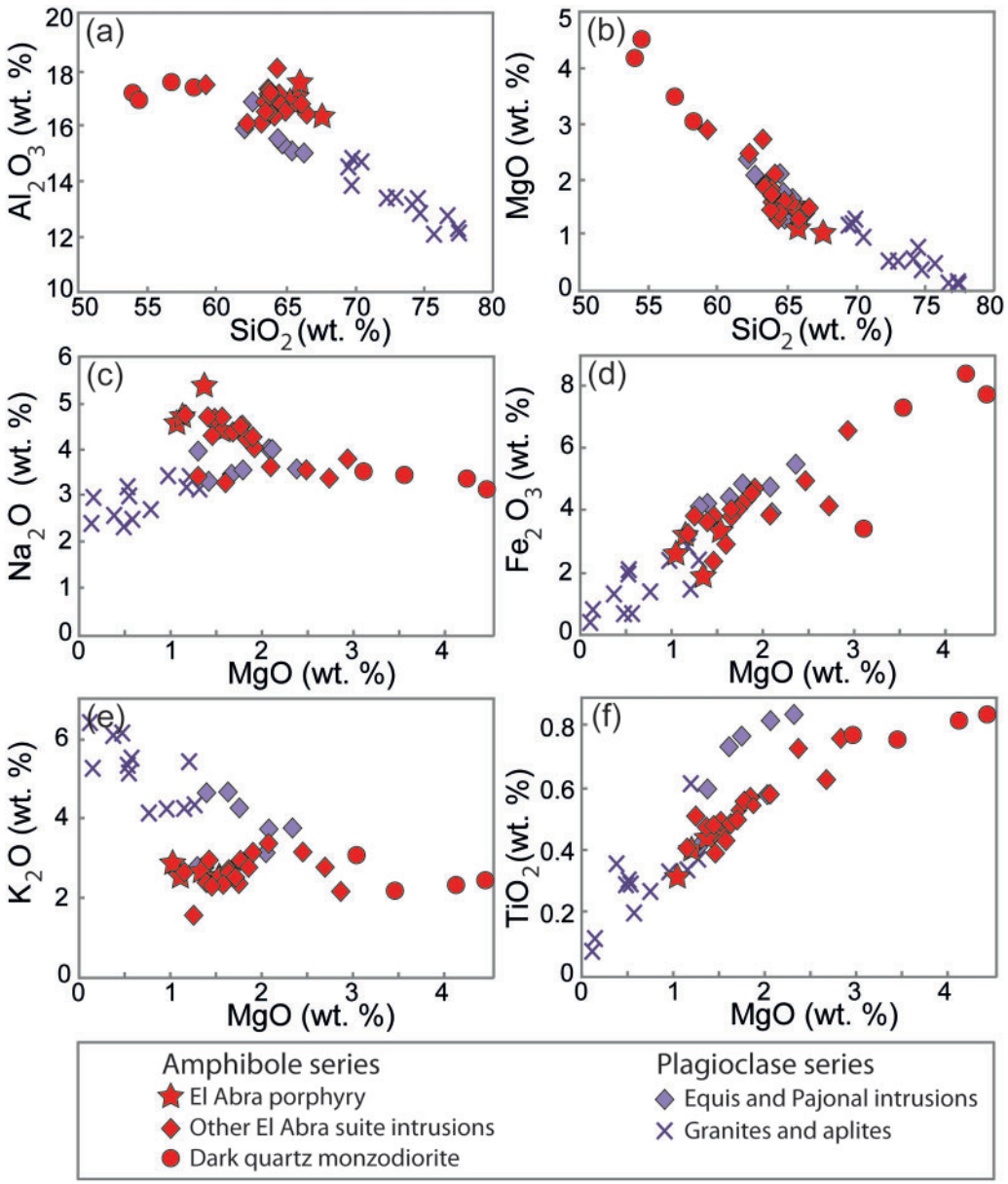

Fig. 4. Selected whole-rock major element variation diagrams for El Abra–Pajonal suite samples. (a, b) Al_2O_3 and MgO vs whole-rock SiO_2; (c–f) Na_2O, Fe_2O_3, K_2O and TiO_2 vs MgO. Red symbols are intrusions younger than 41 Ma and are related to amphibole-dominant fractionation. Star symbols indicate samples from the El Abra porphyry, which is associated with Cu mineralization. Circles are samples from the Dark quartz monzodiorite. Light purple symbols indicate intrusions older than 41 Ma, which are related to plagioclase-dominant fractionation. Crosses are granites and aplites related to plagioclase-dominant fractionation.

agree, within analytical error, with those of samples dated by Ambrus (1977), Dilles *et al.* (1997) and Campbell *et al.* (2006). The ages of the inherited zircons show that the magmas of the El Abra–Pajonal suite sample known stratigraphic and intrusive units in the area. These inherited populations can be correlated with the Eocene Icanche Formation, which consists of andesitic flows and tuffs (Maksaev, 1990; Maksaev *et al.*, 1994; Tomlinson *et al.*, 1995; Ireland, 2010), and the Permian–Triassic Collahuasi Group, which is predominantly made up of interbedded intermediate–felsic volcanic rocks and sedimentary units of sandstone and limestone (Maksaev, 1990; Munizaga *et al.*, 2008).

Magmatic evolution

Although the intrusions that make up the El Abra–Pajonal suite have many similar geochemical characteristics, it is unclear if they have formed predominantly from a single, deeper parent magma that experienced the injection of a more primitive, wetter melt followed by mixing of these magmas, or from separate parent magmas that followed different fractionation trends. As noted above, two distinct series can be recognized, a Plagioclase- and an Amphibole-dominant series. Both evolved through a combination of fractional crystallization and assimilation. New magma batches, originating from the deeper magma chamber(s), were periodically

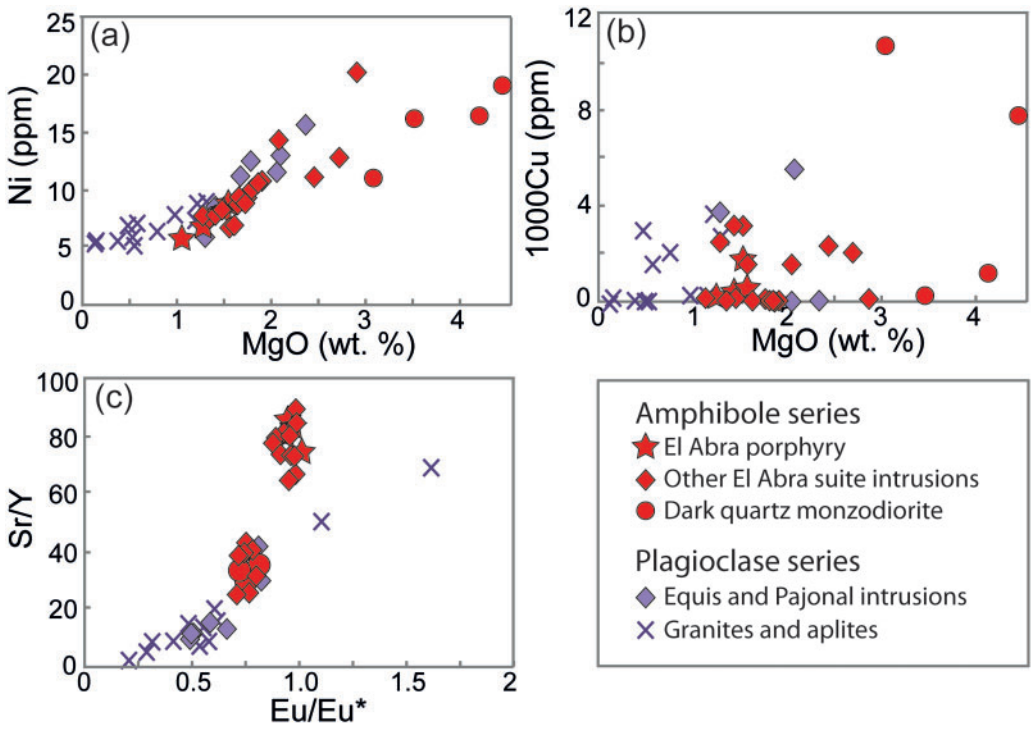

Fig. 5. Selected whole-rock trace element results for El Abra–Pajonal suite samples. (a, b) Ni and 1000Cu vs MgO; (c) Sr/Y vs Eu/Eu*. Symbols as in Fig. 4.

injected into a series of short-lived shallow-crustal magma chambers, from which our samples were collected. Evidence of assimilation, which comes from zircon inheritance and the presence of xenoliths in the intrusions, has been discussed in more detail by Valente (2008).

The older Plagioclase series, which includes the Pajonal quartz monzonite, Equis monzogranite and Antena aplite, shows all the characteristics of plagioclase-dominated fractionation: REE patterns with negative Eu anomalies (i.e. decreasing Eu/Eu*) that correlate with decreasing Sr/Y (Figs 5c and 6b), REE abundances that increase with increasing fractionation, with little change in La/Lu, and Al_2O_3 contents that decrease with increasing SiO_2 (Fig. 4a). Major and trace element modeling by Valente (2008) suggests that pyroxene was the dominant ferromagnesian phase. The Plagioclase series is interpreted to have formed from a relatively dry magma (Annen *et al.*, 2006).

The younger Amphibole series includes the Dark quartz monzodiorite, Central granodiorite, Llareta quartz monzodiorite, Clara granodiorite, El Abra porphyry and Lagarto porphyry. It is characterized by HREE contents that decrease and La/Lu ratios that increase with fractionation, small Eu anomalies that decrease with fractionation (Figs 5c and 6a), and Al_2O_3 that varies little with increasing SiO_2 (Fig. 4a). This type of fractionation is attributed to amphibole-dominated fractionation with little to no plagioclase fractionation from a relatively wet magma (Annen *et al.*, 2006; Richards, 2011*a*; Chiaradia *et al.*, 2012). The spoon-shaped (concave) HREE patterns displayed by these samples are characteristic of amphibole ± titanite fractionation (Ballard, 2001; Valente, 2008).

The exceptions are the Rojo Grande and the Apolo granites, which are clearly the product of plagioclase fractionation but are distinctly younger than the other members of the Plagioclase series. Furthermore, they have the distinctive spoon-shaped HREE patterns of the Amphibole series and clearly belong to that series. Valente (2008) suggested that the fractionation seen in these samples took place in the upper crustal intrusions from which the samples were collected, to explain the compositional variation of samples from the same intrusion, which is appreciably greater than for other members of that series. A drop in pressure, accompanied by loss of water, may explain why plagioclase replaced amphibole as the dominant crystallizing phase. The Apolo granite samples (Fig. 6c) have lower REE abundances and show a wider range of positive and negative Eu anomalies than all other samples, reflecting a combination of plagioclase fractionation and cumulate processes.

The most primitive magma in the El Abra–Pajonal suite is the Dark quartz monzodiorite, which belongs to the Amphibole series. We attribute the Dark quartz monzodiorite to the entry of a new pulse of magma into the system. It is not clear whether this new pulse entered a deep chamber, which contained magma of the Plagioclase series that had been previously been crystallizing plagioclase, and mixed with that magma to produce a magma with an intermediate Eu anomaly, or

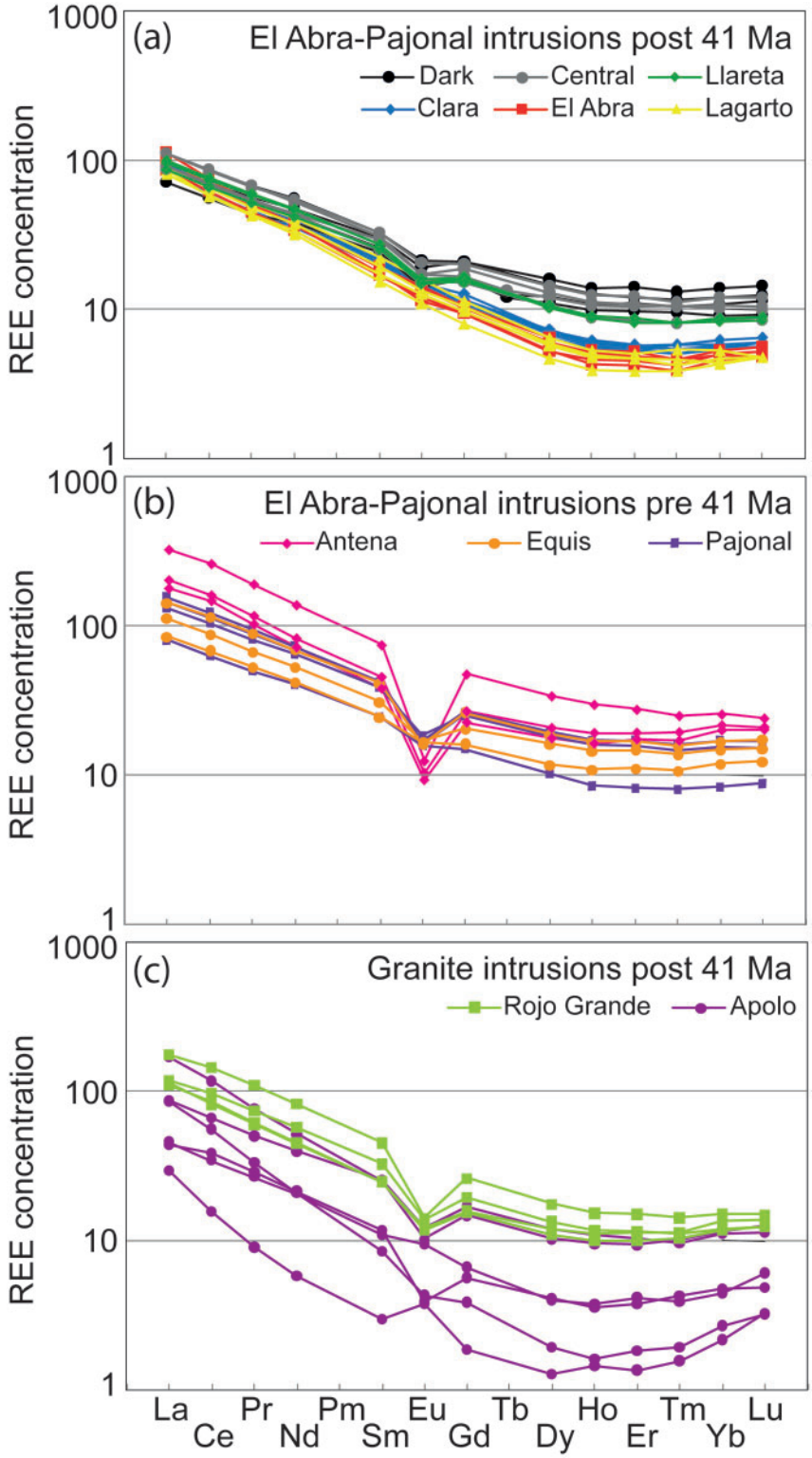

Fig. 6. Cl-normalized whole-rock rare earth element patterns for El Abra–Pajonal intrusion samples. (a) El Abra–Pajonal intrusions that are younger than 41 Ma, excluding granites. (b) El Abra–Pajonal intrusions that are older than 41 Ma. (c) Granite intrusions of the El Abra–Pajonal suite that are younger than 41 Ma.

whether the Amphibole series developed in a deeper chamber that was independent of the first series. The observation that the most primitive magma of the Amphibole series has the strongest Eu anomaly is most simply explained by the former hypothesis. On the other hand, the range of REE concentrations seen in each of the intrusions of the Plagioclase series shows that much of the fractionation occurred within the

Table 3: Whole-rock platinum group element and Re data in ppt for samples and duplicates from the El Abra–Pajonal igneous complex

Sample	Intrusive unit	MgO (wt %)	Cu (ppm)	Ir (ppt)	Ru (ppt)	Rh (ppt)	Pt (ppt)	Pd (ppt)	Re (ppt)
ANU07-115	El Abra porphyry	1·1	292	<0·5	<1·3	<1·4	1188 ± 7·2	301 ± 6·7	1327 ± 5·7
ANU07-115*	El Abra porphyry	1·1		<0·5	<1·3	<1·4	1556 ± 18·5	233 ± 5·9	1443 ± 20·1
ANU07-094	El Abra porphyry	1·1	217	<0·5	<1·3	<1·4	52 ± 7·3	63 ± 7·0	97 ± 4·6
ANU07-094*	El Abra porphyry	1·1		<0·5	<1·3	<1·4	46 ± 7·6	84 ± 5·0	99 ± 5·9
ANU07-105	Equis monzogranite	1·3	3692	<0·5	<1·3	<1·4	76 ± 17·9	66 ± 4·3	139 ± 20·1
ANU07-127	Equis monzogranite	1·4	55	<0·5	<1·3	2·78 ± 0·55	219 ± 8·5	268 ± 8·1	118 ± 3·5
ANU07-127*	Equis monzogranite	1·4		<0·5	<1·3	1·86 ± 0·71	285 ± 7·9	305 ± 7·5	111 ± 5·7
ANU07-098	Clara granodiorite	1·5	89	<0·5	<1·3	<1·4	46 ± 7·2	151 ± 5·5	20 ± 3·3
ANU07-107	El Abra porphyry	1·5	1688	<0·5	16·62 ± 1·17	<1·4	59 ± 7·2	<9·5	9163 ± 88·7
ANU07-107*	El Abra porphyry	1·5		<0·5	8·86 ± 2·02	<1·4	55 ± 7·1	<9·5	11548 ± 51·0
ANU07-085	Clara granodiorite	1·7	13	<0·5	<1·3	<1·4	55 ± 7·2	123 ± 6·0	<8·2
ANU07-085*	Clara granodiorite	1·7		<0·5	<1·3	<1·4	49 ± 7·2	144 ± 4·5	<8·2
ANU07-082	Pajonal quartz monzonite	1·8	43	1·89 ± 0·24	<1·3	8·23 ± 0·72	408 ± 8·0	226 ± 5·7	119 ± 5·3
ANU07-089	Llareta quartz monzodiorite	1·8	30	<0·5	<1·3	<1·4	145 ± 7·5	152 ± 6·8	77 ± 3·1
ANU07-089*	Llareta quartz monzodiorite	1·8		<0·5	<1·3	<1·4	157 ± 8·2	162 ± 5·1	79 ± 3·7
ANU07-093	Llareta quartz monzodiorite	1·9	14	<0·5	<1·3	<1·4	126 ± 7·9	136 ± 5·5	114 ± 4·5
ANU07-092	Pajonal quartz monzonite	2·1	58	<0·5	<1·3	2·39 ± 0·54	353 ± 9·6	183 ± 5·4	26 ± 3·2
ANU07-092*	Pajonal quartz monzonite	2·1		1·88 ± 0·18	<1·3	9·90 ± 1·56	591 ± 11·7	808 ± 7·9	73 ± 3·5
ANU07-104	Central granodiorite	2·1	1445	<0·5	<1·3	2·06 ± 0·54	341 ± 10·8	429 ± 9·3	17248 ± 167·0
ANU07-104*	Central granodiorite	2·1		<0·5	1·39 ± 0·67	<1·4	984 ± 15·1	400 ± 10·3	22082 ± 230·8
ANU07-110	Equis monzogranite	2·1	5493	1·73 ± 0·18	2·30 ± 0·53	5·90 ± 0·56	776 ± 10·6	212 ± 5·4	403 ± 10·6
ANU07-110*	Equis monzogranite	2·1		1·87 ± 0·26	<1·3	3·60 ± 0·84	784 ± 9·9	253 ± 6·1	415 ± 11·8
Sample	Intrusive unit	MgO (wt %)	Cu (ppm)	Ir (ppt)	Ru (ppt)	Rh (ppt)	Pt (ppt)	Pd (ppt)	Re (ppt)
ANU07-122*	Pajonal quartz monzonite	2·4		<0·5	<1·3	2·95 ± 0·77	418 ± 8·7	423 ± 6·5	30 ± 3·2
ANU07-122	Pajonal quartz monzonite	2·4	72	5·38 ± 0·23	<1·3	11·17 ± 0·67	604 ± 10·4	797 ± 19·3	91 ± 3·2
ANU00-131†	Central granodiorite	2·5		1·31 ± 0·30	2·54 ± 1·24	10·63 ± 0·75	1017 ± 29·7	1075 ± 32·2	5770 ± 179·7
ANU07-113	Central granodiorite	2·7	2135	1·29 ± 0·17	2·50 ± 0·58	4·14 ± 0·76	457 ± 10·4	883 ± 71·4	46780 ± 891·0
ANU07-113*	Central granodiorite	2·7		26·97 ± 0·86	<1·3	4·14 ± 0·88	518 ± 13·0	961 ± 15·7	29729 ± 549·3
ANU07-103	Central granodiorite	2·9	50	1·13 ± 0·18	<1·3	5·02 ± 0·53	467 ± 12·7	848 ± 18·6	15933 ± 290·2
ANU07-103*	Central granodiorite	2·9		<0·5	<1·3	6·22 ± 1·10	585 ± 11·5	771 ± 15·0	18241 ± 155·45
ANU00-180†	Dark quartz monzodiorite	3·1		0·56 ± 0·17	<1·3	29·27 ± 2·34	635 ± 18·2	618 ± 47·9	3234 ± 80·1
ANU07-101	Dark quartz monzodiorite	3·5	293	0·62 ± 0·15	<1·3	3·96 ± 0·53	699 ± 15·9	804 ± 14·7	6080 ± 117·1
ANU07-101*	Dark quartz monzodiorite	3·5		<0·5	<1·3	4·09 ± 0·87	570 ± 12·0	886 ± 17·1	6872 ± 106·2
ANU07-108	Dark quartz monzodiorite	4·2	1168	2·15 ± 0·27	<1·3	4·17 ± 0·56	705 ± 12·6	1940 ± 31·9	189 ± 6·9
ANU07-108*	Dark quartz monzodiorite	4·2		<0·5	<1·3	4·00 ± 0·89	738 ± 12·4	1995 ± 19·4	145 ± 4·3
ANU00-182†	Dark quartz monzodiorite	4·5		2·01 ± 0·19	2·86 ± 1·19	10·65 ± 0·79	848 ± 15·7	1377 ± 34·1	227 ± 11·5

*Duplicate samples that also incorporated the Te co-precipitation method.
†MgO and Cu data are from Ballard (2001).
Errors are the total combined uncertainties in the data, which primarily result from uncertainty in the blank subtraction and ICP-MS counting statistics.

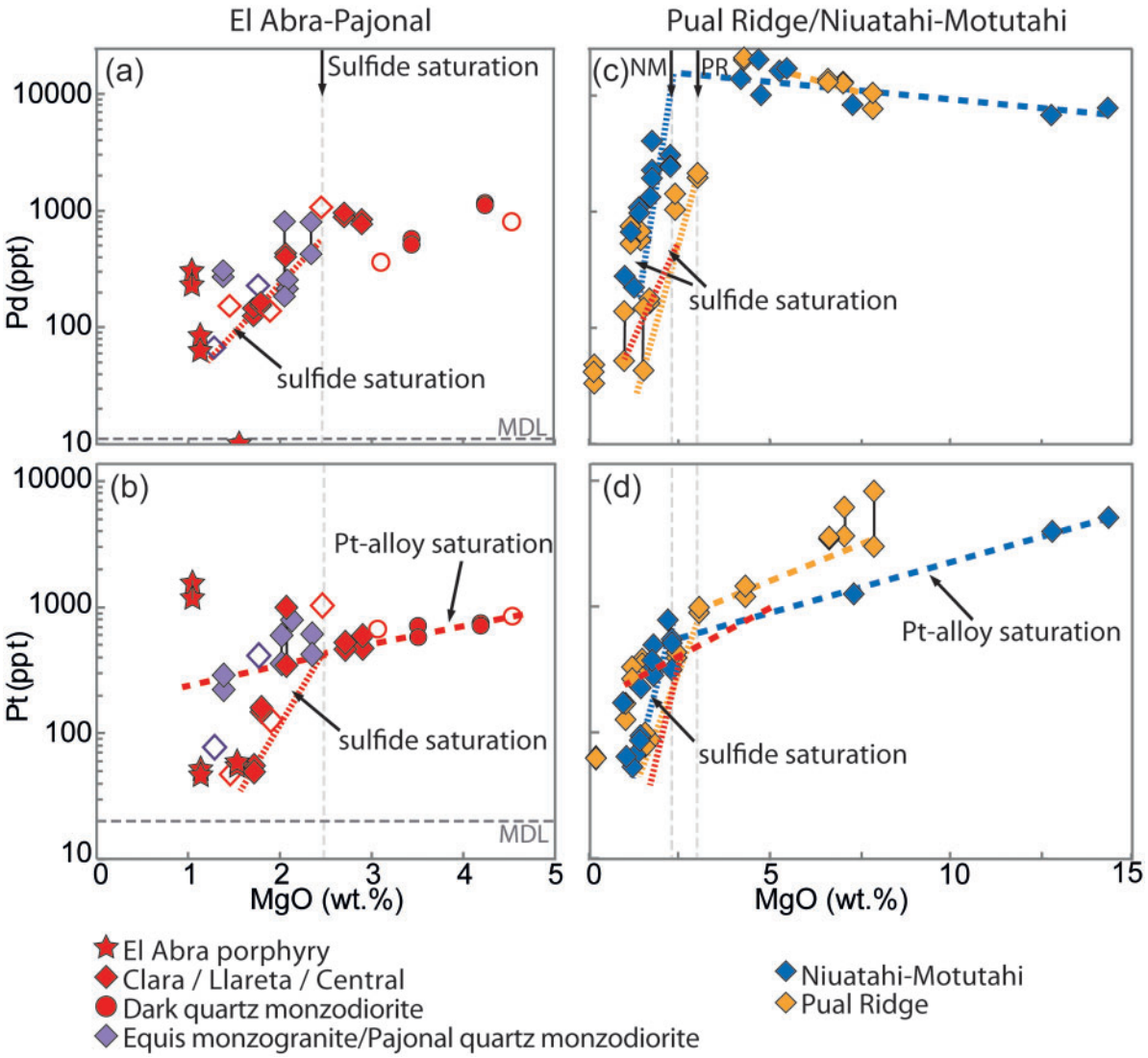

Fig. 7. Variation of Pd (a, c) and Pt (b, d) vs MgO for samples from the El Abra–Pajonal igneous complex and for Pual Ridge and Niuatahi–Motutahi suites (Park *et al.*, 2013a, 2015) for comparison. Red symbols are intrusions younger than 41 Ma and are related to amphibole-dominant fractionation. Star symbols indicate samples from the El Abra porphyry, which is associated with Cu mineralization. Circles are samples from the Dark quartz monzodiorite. Light purple symbols indicate intrusions older than 41 Ma, which are related to plagioclase-dominant fractionation. Open symbols show samples that were not analysed in duplicate. Dashed lines show Pt trends prior to sulfide saturation; dotted lines show Pd and Pt trends after sulfide saturation. Continuous vertical lines link duplicate samples (see Table 3 for more details of duplicate analyses). MDL, method detection limit.

sampled upper-level intrusions. As with the Rojo Grande and Apolo intrusions, loss of water during decompression may explain why amphibole crystallization is unimportant or absent in the Plagioclase series. In either case the PGE geochemistry of the two series needs to be treated separately.

Amphibole fractionation can be characterized by depletion of elements such as Fe, Mg, Ti, Al, Ca, Ni and Y, along with depletion of the middle REE (MREE; e.g. Dy) (Table 2; Figs 4, 5 and 6a; Supplementary Data Fig. A1; Bottazzi *et al.*, 1999). Rohrlach (2005) proposed that the Sr/Y ratio can be used to measure the relative importance of plagioclase versus amphibole fractionation in evolving magmas and therefore to establish if the magmas are hydrous or anhydrous because Sr is preferentially partitioned into plagioclase, which is favored by dry magmas, and Y into hornblende, which crystallizes from wet magmas. Therefore magmatic systems in which amphibole fractionation dominates over plagioclase will produce melts with successively higher Sr/Y and La/Yb values (Figs 5c and 8b; Rohrlach, 2005; Richards, 2011*a*). Amphibole-dominant fractionation in the deeper parent magma chamber, which fed the smaller higher-level chambers of the Amphibole series we have sampled, is marked by continuously increasing La/Dy and La/Yb (Fig. 6) and decreasing Dy, Y, Ni, Fe and Mg concentrations. These observations suggest that amphibole fractionation became increasingly important in the magmatic system from 41·7 Ma, peaking with the emplacement of the Clara granodiorite and the

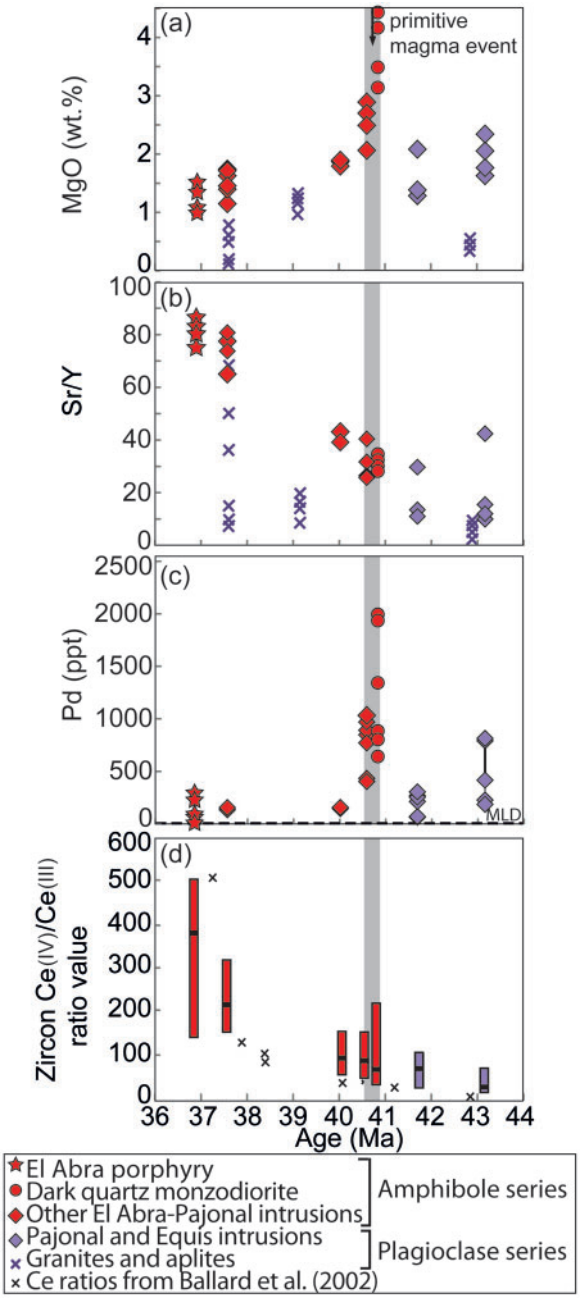

Fig. 8. (a) Whole-rock MgO (wt %), (b) Sr/Y, (c) Pd (ppb) and (d) zircon Ce^{4+}/Ce^{3+} ratios vs average U–Pb zircon ages of the intrusions of the El Abra–Pajonal igneous complex. Symbols are as in Fig. 4.

porphyries, which are depleted in MREE to HREE and have very small or no Eu anomalies compared with the older intrusive units of the Amphibole series (Fig. 6a). We attribute the increasing Eu/Eu* to plagioclase accumulation, which also increases Sr/Y, and the bimodal distribution as discriminating between intrusions that accumulated plagioclase phenocrysts, such as the Clara granodiorite, El Abra porphyry and Lagarto porphyry, and those that did not, such as the Dark quartz monzodiorite and Central granodiorite. The obvious inference of the increasing importance of amphibole in the magma system is that the deep parent magma chamber became increasingly hydrous and thus a greater amount of water exsolved in the shallow-level chambers, leading eventually to the formation of the magmatic hydrothermal fluids that produced the El Abra porphyry mineralization. These trends contrast sharply with those seen in the Plagioclase series, which are produced by relatively dry magmas. It should be noted that the higher Sr/Y seen in the Apolo granite samples (which have corresponding Eu/Eu* >1) relative to the other granites is due to plagioclase accumulation rather than fractional crystallization. Pyroxene, although seen in only trace amounts in the Pajonal quartz monzonite, is also a likely cumulate phase in the plagioclase-dominated parent chamber of the intrusions older than 41 Ma.

PGE-alloy and sulfide saturation

Samples with MgO >2·5 wt % show a steady decrease in Pt abundance with decreasing MgO content, as is typical of a magma that is saturated with a Pt-rich metal alloy, but not with a sulfide melt (Fig. 7d; Park *et al.*, 2013a However, there is no clear trend in Pd for samples with MgO >2·5 wt %, which is different from the well-defined trends seen in the Paul Ridge and Niuatahi–Motutahi data (Fig. 7c). This difference is attributed to the Paul Ridge and Niuatahi–Motutahi samples being fine-grained or glassy lavas, representing melts, whereas those from El Abra–Pajonal are phenocryst-bearing porphyritic to phaneritic plutonic rocks collected from shallow-level intrusions. Evidence of fractionation occurring within single intrusions (Figs 4–6) provides clear indication that cumulate processes were operating in the deep magma chamber. Prior to sulfide saturation, Pd behaves as an incompatible element (Park *et al.*, 2013a) and its concentration in cumulate rocks is controlled by a combination of its concentration in the melt and the fraction of trapped liquid in the cumulate rock. We suggest that the absence of a clear trend in the El Abra–Pajonal Pd data, owing to the expected increase in the Pd content of the melt (compare Fig. 7a and c), is obscured by variations in the amount of trapped liquid in the cumulate rocks. Alternatively, lack of a clear trend in the pre-sulfide Pd data could be due to subtle magma mixing that cannot be unambiguously identified in the major or trace element data. Over the same MgO interval Pt follows a well-defined trend because it is precipitating as a cumulus Pt-rich alloy and is less affected by the amount of trapped liquid in the rocks. Its decline in Fig. 7b and d is controlled mainly by the declining solubility of Pt in the cooling melt.

Depletion in Pt, without a corresponding decline in Pd, is attributed to alloy precipitation (Park *et al.*, 2013a, 2015). The fraction required to produce the observed decline in Pt in samples with MgO >2·5 wt % is very small (Fig. 7b). Because the rate of decline of Pt in the melt is low, the bulk partition coefficient must be only

slightly greater than unity. If we assume that the alloy contains *c.* 85% Pt, as expected for an alloy precipitating from a felsic melt (Park *et al.*, 2013a), the fraction of alloy needed to produce the observed Pt decline from 700 to 450 ppt (from 4·2 to 2·7 wt % MgO) is *c.* 8 ppb, assuming that 30% fractionation is required to produce the observed drop in MgO. The scatter in duplicate analyses of samples with MgO contents greater than 2·5% is greater for Pt than Pd, which is consistent with the existence of a Pt-rich alloy, because the presence of these alloys affects the Pt but not Pd concentrations (see Park *et al.*, 2013a).

Below *c.* 2·5 wt % MgO the Pt and Pd concentrations in the El Abra samples decrease rapidly, which we attribute to the melts reaching sulfide saturation. This is best seen in the Amphibole series, which gave rise to the ore-associated El Abra porphyry. As noted above, most of the fractional crystallization at El Abra is interpreted to have occurred in a deep parent magma, which underlay the shallow daughter intrusions that were sampled for this study, whereas the ore-forming fluids emanated from one of the shallow daughter intrusions, the El Abra porphyry. As a consequence, the ore-forming fluids did not have access to the cumulate sulfides in the deep parent magma chamber. In this context we note that the cumulus sulfides of the Merensky and Platinova Reefs of the Bushveld and Skaergaard intrusions, respectively (Barnes & Campbell, 1988; Keays & Tegner, 2015), and Opirarukaomappu Gabbroic Complex of Japan (Tomkins *et al.*, 2012) preserve their cumulate sulfides at depth with no evidence of having lost either Cu or Au. Furthermore, if magmatic sulfides were contributing to the ore fluid, one might expect a correlation between Cu and Pd. A plot of Cu against Pd for the analyzed El Abra samples (Supplementary Data Fig. A2) shows no such correlation. Plots of Cu (Fig. 5b) and Au (not shown) versus MgO, prior to sulfide saturation (before the appearance of sulfide nuggets), show appreciably more scatter than the PGE plots, which supports the conclusion that Cu and Au are more mobile than the PGE. The decreases in Pt and Pd seen in this series are similar to those seen at Pual Ridge and Niuatahi–Motutahi (Fig. 7c and d), which are also attributed to sulfide saturation (Park *et al.*, 2013*a*, 2015). Once sulfide saturation was reached at 2·5 wt % MgO the Pt concentration of the samples fell below the Pt solubility curve as obtained by projecting the pre-sulfide Pt solubility curve beyond sulfide saturation (Fig. 7b). Prior to sulfide saturation at 2·5 wt % MgO only the Pt data show scatter in the duplicate analyses, whereas for samples with $<$2·5 wt % MgO both Pt and Pd show scatter. We attribute this difference to the presence of an immiscible sulfide melt, which sequesters both Pt and Pd, replacing the Pt-rich metal alloy as the nugget phase precipitating from the melt.

The presence of nuggets complicates the interpretation of the post-sulfide saturation trend line shown in Fig. 7a and b. This means that the analyzed samples have two components, a solidified melt component and a nugget (or cumulate) component. The post-sulfide saturation melt component is best evaluated by drawing the trend line through the lowest points in Fig. 7a and b to minimize the nugget effect. We have done this, but because there is no certainty that even the low Pt–Pd points contain no nuggets, the trend line may have a slope that is lower than the true liquid fractionation trend.

The disagreement in Pt and Pd values for duplicates from the Plagioclase series samples, which is greater than that seen in the Amphibole series, is attributed to a higher abundance of sulfide nuggets. The absence of clear trends in this series is also attributed to the abundance of nuggets. Although no trends can be recognized, the presence of sulfide nuggets requires all samples from the Plagioclase series intrusions to have crystallized from a sulfide-saturated melt.

Significant and conclusive petrographic evidence of PGE-alloys and sulfide melt in the El Abra–Pajonal suite samples is lacking because the amount of alloy or sulfide required to produce the observed effect is miniscule, which makes them difficult to find by optical microscopy. Furthermore, most of the alloys and sulfide precipitates are postulated to form in an unexposed deeper magma chamber below the sampled shallow intrusions. Sulfide melt blebs associated with sulfide saturation in an evolving magmatic system have been identified in other intrusive suites; for example, the Boggy Plains pluton (Park *et al.*, 2013*b*). In reflected light, yellow inclusions in phenocrysts of possible primary origin, which are rare and too small to identify with confidence, occur in several of the El Abra–Pajonal suite units (El Abra porphyry, Clara granodiorite, Central granodiorite, Dark quartz monzodiorite, Equis monzogranite). These could be sulfide melt blebs that may have formed in the deeper magma chamber and been incorporated into the sampled high-level intrusions in phenocrysts.

A sample of the El Abra porphyry with 1·1 wt % MgO (Fig. 7b) is anomalous with very high Pt but only slightly elevated Pd, indicating that the anomaly is due to the presence of nuggets of Pt-rich metal alloy and not an immiscible sulfide. This interpretation is consistent with the marked difference in the Pt duplicates. If the anomalous Pt values are due to nuggets they must come from the deep chamber, probably as inclusions in early formed phenocrysts, because the sample that contains them formed well after sulfide saturation. Park *et al.*, (2013a) also noted a correlation between the presence of phenocrysts and metal alloy nuggets at Pual Ridge.

The El Abra porphyry Cu deposit formed towards the end of the magmatic evolution of the intrusive system. Whole-rock MgO values for the El Abra porphyry, which is the unit associated with the mineralizing event, range from 1·05 to 1·54 wt %, which is at least 1·0 wt % MgO less than the MgO content at which sulfide saturation occurred. Despite the occurrence of sulfide saturation prior to ore-fluid saturation, Cu was available to partition into the ore-fluid phase and form the Cu deposit.

This is possible only if the amount of sulfide liquid that formed at sulfide saturation was small. The sulfide melt–silicate melt partition coefficient of Cu (10^2–10^3) is lower than that of Au (10^3–10^4), and much lower than that for Pt and Pd (*c.* 10^5–10^6) (Campbell & Barnes, 1984; Ripley *et al.*, 2002; Fonseca *et al.*, 2009; Mungall & Brenan, 2014), allowing the sulfide liquid to strip the magma of Au and PGE but not Cu. Richards (2005) recognized that fractionation of a small amount of sulfide melt would remove Au from the silicate melt but not significantly affect its Cu content; the results of this study are consistent with this hypothesis. Therefore both the timing of sulfide saturation relative to ore-fluid saturation and the amount of sulfide melt are important. Where sulfide saturation preceded ore-fluid saturation it is the amount of sulfide melt that formed that controls the Cu and Au content of the silicate melt and therefore whether the magmatic system has the potential to produce an ore deposit and, if it does, whether the deposit that forms is Cu-only or Cu–Au.

Sulfide saturation in porphyry systems is suggested to have occurred at other deposits; for example, Bajo de la Alumbrera, Argentina, and Bingham Canyon, Utah (Keith *et al.*, 1997; Halter *et al.*, 2002, 2005). These studies, along with review papers, have proposed that the sulfide droplets that form at sulfide saturation subsequently break down and release chalcophile elements into exsolving fluids that form the porphyry deposits (Richards, 2009, 2011*b*; Audétat & Simon, 2012; Wilkinson, 2013). However, this does not appear to be the case at El Abra, nor for the magma chambers that are interpreted to underlie the Pual Ridge and Niuatahi–Motutahi volcanic areas (Fig. 7c and d), because in all cases the Pt and Pd abundances fall following sulfide saturation in a deeper magma chamber. In addition, there is no correlation between Cu and Pd at El Abra (Supplementary Data Fig. A2), as would be expected if sulfide droplets broke down and released the chalcophile elements into hydrothermal fluids, because the amount of sulfide melt that formed in the deeper chamber was very small, removing PGE and Au from the melt but not significant Cu, allowing the Cu to partition into the hydrothermal fluids that exsolved to form the El Abra porphyry Cu deposit.

Although there are many factors that can influence the nature of porphyry mineralization, our study focuses on the role of sulfide saturation and its impact on porphyry Cu ± Au deposits. The geodynamic setting and the alkalinity of the magmas may also play a role in determining Cu:Au ratios in some porphyry systems and these have been discussed in more detail by Sillitoe (1997) and Richards (2009). Gold-rich porphyries are typically associated with more alkaline magmas, for example the Cu–Au porphyries in New South Wales, Australia (Wilson *et al.*, 2003; Cooke *et al.*, 2007; Lickfold *et al.*, 2007), which form in post-subduction settings. In contrast, Cu-rich porphyries are often related to intrusions of weakly alkaline to subalkaline affinities that are associated with active subduction (Sillitoe, 2010). The El Abra–Pajonal suite intrusions are subalkaline magmas associated with subduction.

Relative oxidation state of the magmas

Changes in the Ce^{4+}/Ce^{3+} in zircon suggest that the magmas of the Amphibole series became more oxidized as the suite evolved (Fig. 8d); we estimate the f_{O2} of the suite to be near that of the sulfide–sulfate transition. These results are consistent with those of Ballard *et al.* (2002) for samples from the same suite (shown as small black crosses in Fig. 8d). As noted above, the oxidation state of the melt has an important influence on the solubility of sulfur. The stable species of sulfur in oxidized magmas is sulfate, which dissolves readily in silicate melts, whereas in reduced melts the stable form is the less soluble sulfide. We suggest that late sulfide saturation in the Amphibole series is due to the magma becoming increasingly oxidized with fractionation, and that this partially offsets the effect of declining temperature in the cooling parent magma chamber that is interpreted to underlie the El Abra suite of intrusions. We note too that the El Abra suite follows a monotonic Fe depletion trend so that there is no 'magnetite crisis', which leads to a sudden drop in the oxidation state and precipitation of sulfides, as seen at Pual Ridge (Jenner *et al.*, 2010). For these reasons the increase in the oxidation state of the Amphibole-series melts with fractionation increased the likelihood of them forming an economic Cu deposit.

Sulfide saturation modeling

The theoretical effects of sulfide saturation have been modeled using the Rayleigh fractionation equation and assuming that the partition coefficients (*D*) for the partitioning of Cu, Au and Pt–Pd between immiscible sulfide and silicate melts are $1{\cdot}5 \times 10^3$, 10^4 and 2×10^5, respectively (Ripley *et al.*, 2002; Fonseca *et al.*, 2009; Mungall & Brenan, 2014). The models assume that the rate of sulfide precipitation increases gradually over a 10% interval, as observed by Keays & Tegner (2015) for Skaergaard, starting at 70% fractionation, and are shown in Fig. 9. It should be noted that the rate of decline of Cu, Au, and the PGE is in order of their partition coefficients, as expected. Although there is some uncertainty as to the exact *D* values, these do not affect the conclusions drawn here, provided the relative order of $D_{Cu} < D_{Au} < D_{PGE}$ is correct, because the differences between them are so large (e.g. order of magnitude variations). If the *D* values are lower than the assumed values, more sulfide precipitation is needed to produce the bulk *D* values required to explain our data; if they are higher, less sulfide precipitation is required.

At 80% fractionation, if the sulfide melt makes up 1% of the fractionating phases, the Cu, Au and PGE content of the melt will be small to negligible (Fig. 9). A fluid emanating from such a magma would be barren. Alternatively, if the sulfide melt makes up 0·3% of the fractionating phases most of the Au and PGE will be

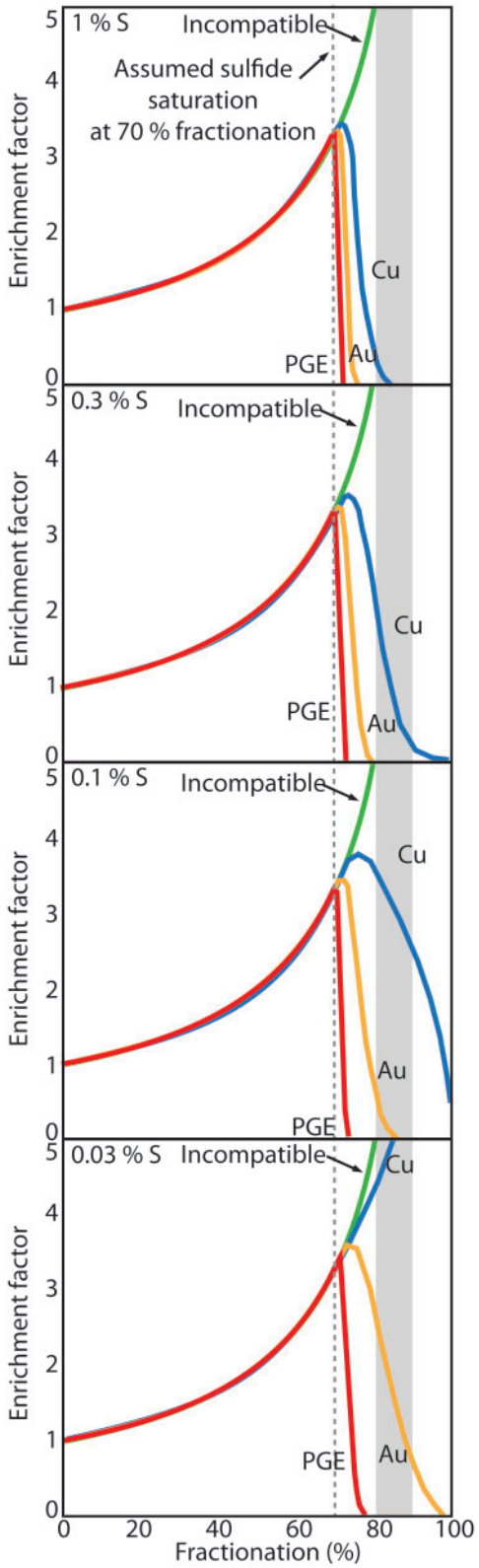

Fig. 9. Concentrations of Cu (blue), incompatible elements (green), Au (orange), and PGE (red) vs per cent fractionation. Sulfide saturation is assumed to occur at 70% fractionation for various percentages of sulfide melt formed. $D^{\text{sulfide melt/silicate melt}}$ values used are $1{\cdot}5 \times 10^3$ for Cu, 10^4 for Au, and 2×10^5 for PGE (see text for details). Shaded grey band indicates 80–90% fractionation; this is used in the text discussion of ore-fluid saturation.

removed but only *c.* 50% of the Cu (Fig. 9). If ore-fluid saturation occurred at 80% fractionation, the mineralizing fluid would be Cu-rich and Au-poor, and would produce Cu-only mineralization. If sulfide fractionation is reduced to 0·1%, the Cu content of the melt falls much more gradually following sulfide saturation. However, the Au content continues to fall rapidly, becoming negligible by 80%. A fluid forming at 80% fractionation is expected to form a deposit that is richer in Cu than the previous case, but still Au poor. We suggest that this is the case at El Abra and can explain why El Abra is a Cu-only deposit. A Cu–Au deposit will develop only if the amount of sulfide melt to form is well below 0·03% or if ore-fluid saturation occurs before or very soon after sulfide saturation. The rate of sulfide melt precipitation is probably controlled by a combination of the cooling rate of the magma and the rate at which its oxidation state changes.

CONCLUSIONS

Mean U–Pb zircon ages and whole-rock and mineral chemistry data for the El Abra–Pajonal suite intrusions indicate that the El Abra–Pajonal magmas evolved in a long-lived, mid- to lower-crustal magma chamber over a period from 43 to 35 Ma. New magma batches, originating from this mid-crustal chamber, were periodically injected into a series of short-lived upper-crustal chambers with a periodicity of *c.* 1 Myr. Fractional crystallization and assimilation, along with injection of mafic magma at 41–40 Ma, were the key magmatic processes governing the evolution of the El Abra–Pajonal suite, producing a suite of alkali feldspar granite to quartz monzodiorite intrusions. The intrusions older than 41 Ma formed by plagioclase-dominant fractionation of relatively dry magmas, whereas the younger intrusions of the Amphibole series formed by amphibole-dominant fractionation of wetter magmas. The oxidation state and water content of the Amphibole series increased with fractionation, the former leading to delayed sulfide saturation and the latter promoting early saturation of a hydrothermal fluid. This combination favored the formation of the fertile magmatic–hydrothermal fluid associated with formation of the El Abra porphyry Cu deposit.

Sulfide saturation occurred before ore-fluid saturation during the evolution of the El Abra–Pajonal igneous complex. However, the system still produced a Cu deposit because the amount of immiscible sulfide melt precipitation was very small, enough to strip most of the PGE and Au from the silicate melt but only a fraction of the Cu. As a consequence, the El Abra–Pajonal igneous complex produced a Cu-rich, Au-poor ore body. The timing and extent of sulfide saturation in a porphyry system not only influences whether ore mineralization occurs but may also affect the type of mineralization that forms, whether it is Cu, Cu–Au or PGE-enriched Cu–Au.

ACKNOWLEDGEMENTS

We would like to thank Andres Molina Hidalgo and Jeff Gerwe from El Abra S.C.M., Chile, for sampling and field assistance, and Charlotte Allen for ICP-MS assistance. We thank Andreas Audétat, Steve Barnes and Marjorie Wilson for their comments in reviewing this paper.

SUPPLEMENTARY DATA

Supplementary data for this paper are available at *Journal of Petrology* online.

REFERENCES

Ambrus, J. (1977). Geology of the El Abra porphyry copper deposit, Chile. *Economic Geology* **72**, 1062–1085.

Annen, C., Blundy, J. D. & Sparks, R. S. J. (2006). The genesis of intermediate and silicic magmas in deep crustal hot zones. *Journal of Petrology* **47**, 505–539.

Audétat, A. & Simon, A. C. (2012). Magmatic controls on porphyry copper genesis. In: Hedenquist, J. W., Harris, M. & Camus, F. (eds) *Geology and Genesis of Major Copper Deposits and Districts of the World: A Tribute to Richard H. Sillitoe. Society of Economic Geologists, Special Publication* **16**, 553–572.

Ballard, J. R. (2001). A comparative study between the geochemistry of ore-bearing and barren calc-alkaline intrusions. PhD thesis, Australian National University, Canberra, ACT, 255 pp.

Ballard, J. R., Palin, J. M. & Campbell, I. H. (2002). Relative oxidation states of magmas inferred from Ce(IV)/Ce(III) in zircon: application to porphyry copper deposits of northern Chile. *Contributions to Mineralogy and Petrology* **144**, 347–364.

Barnes, S. J. & Campbell, I. H. (1988). Role of late magmatic fluids in Merensky-type platinum deposits: A discussion. *Geology* **16**, 488–491.

Barrett, L. F. (1997). El Abra district map, scale 1:250,000. Unpublished company map. Calama: S.C.M. El Abra.

Barrett, L. F. (2004). Geology and status of exploration projects, El Abra District, II Region, Chile. Unpublished company report. Calama: S.C.M. El Abra, pp. 6–37.

Black, L. P., Kamo, S. L., Allen, C. M., Davis, D. W., Aleinikoff, J. N., Valley, J. W., Mundil, R., Campbell, I. H., Korsch, R. J., Williams, I. S. & Foudoulis, C. (2004). Improved $^{206}Pb/^{238}U$ microprobe geochronology by the monitoring of a trace-element-related matrix effect; SHRIMP, ID-TIMS, ELA-ICP-MS and oxygen isotope documentation for a series of zircon standards. *Chemical Geology* **205**, 115–140.

Bottazzi, P., Tiepolo, M., Vannucci, R., Zanetti, A., Brumm, R., Foley, S. F. & Oberti, R. (1999). Distinct site preferences for heavy and light REE in amphibole and the prediction of $^{Amph/L}D_{REE}$. *Contributions to Mineralogy and Petrology* **137**, 36–45.

Campbell, I. H. & Barnes, S. J. (1984). A model for the geochemistry of the platinum-group elements in magmatic sulfide deposits. *Canadian Mineralogist* **22**, 151–160.

Campbell, I. H., Ballard, J. R., Palin, J. M., Allen, C. & Faunes, A. (2006). U–Pb zircon geochronology of granitic rocks from the Chuquicamata–El Abra porphyry copper belt of northern Chile: excimer laser ablation ICP-MS analysis. *Economic Geology* **101**, 1327–1344.

Candela, P. A. (1997). A review of shallow, ore-related granites: textures, volatiles, and ore metals. *Journal of Petrology* **38**, 1619–1633.

Chiaradia, M., Ulianov, A., Kouzmanov, K. & Beate, B. (2012). Why large porphyry Cu deposits like high Sr/Y magmas? *Scientific Reports* **2**, electronic publication, 24 September.

Cooke, D. R., Hollings, P. & Walsh, J. L. (2005). Giant porphyry deposits: Characteristics, distribution, and tectonic controls. *Economic Geology* **100**, 801–818.

Cooke, D. R., Wilson, A. J., House, M. J., Wolfe, R. C., Walshe, J. L., Lickfold, V. & Crawford, A. J. (2007). Alkalic porphyry Au–Cu and associated mineral deposits of the Ordovician to Early Silurian Macquarie Arc, New South Wales. *Australian Journal of Earth Sciences* **54**, 445–463.

Cornejo, P. C., Tosdal, R. M., Mpodozis, C., Tomlinson, A. J., Rivera, O. & Fanning, C. M. (1997). El Salvador, Chile porphyry copper deposit revisited; geologic and geochronologic framework. *International Geology Review* **39**, 22–54.

Dilles, J. H. (1987). Petrology of the Yerington Batholith, Nevada: evidence for evolution of porphyry copper ore fluids. *Economic Geology* **82**, 1750–1789.

Dilles, J. H., Tomlinson, A. J., Martin, M. W. & Blanco, N. (1997). El Abra and Fortuna complexes: a porphyry copper batholith sinistrally displaced by the Falla Oeste. Unpublished company report. Actualización del conocimiento geológico de Chuquicamata, 1, Publicaciones de Geología, CODELCO Chile, División Chuquicamata, pp. 11–15.

Economou-Eliopoulos, M. (2005). Platinum-Group Element potential of porphyry deposits. In: Mungall, J. E. (ed.) *Exploration for Platinum-Group Elements Deposits. Mineralogical Association of Canada, Short Course Series* **35**, 203–245.

Fonseca, R. O. C., Campbell, I. H., O'Neill, H. S. C. & Allen, C. M. (2009). Solubility of Pt in sulphide mattes: Implications for the genesis of PGE-rich horizons in layered intrusions. *Geochimica et Cosmochimica Acta* **73**, 5764–5777.

Garza, R. A. P., Titley, S. R. & Pimentel, F. (2001). Geology of the Escondida porphyry copper deposit, Antofagasta region, Chile. *Economic Geology and Bulletin of the Society of Economic Geologists* **96**, 307–324.

Gerwe, J. (2005). The El Abra porphyry copper deposit: An overview. Unpublished company presentation. S.C.M. El Abra.

Graichen, R. E., Dean, D. A., Barrett, L. F., Burton, W. D. & Christenson, D. K. (1995). Geologic overview of the El Abra porphyry copper deposit, Chile. Unpublished company report. Cyprus Amax Minerals Company, Phoenix, Arizona, pp. 1–11.

Halter, W., Heinrich, C. & Pettke, T. (2005). Magma evolution and the formation of porphyry Cu–Au ore fluids: evidence from silicate and sulfide melt inclusions. *Mineralium Deposita* **39**, 845–863.

Halter, W. E., Pettke, T. & Heinrich, C. A. (2002). The origin of Cu/Au ratios in porphyry-type ore deposits. *Science* **296**, 1844–1846.

Harris, A. C., Allen, C. M., Bryan, S. E., Campbell, I. H., Holcombe, R. J. & Palin, J. M. (2004). ELA-ICP-MS U–Pb zircon geochronology of regional volcanism hosting the Bajo de la Alumbrera Cu–Au deposit: implications for porphyry-related mineralization. *Mineralium Deposita* **39**, 46–67.

Ireland, T. (2010). Geological framework of the mineral deposits of the Collahuasi district, Región de Tarapacá, Chile. Ph.D. thesis, University of Tasmania, 414 pp.

Jackson, S. E., Fryer, B. J., Gosse, W., Healey, D. C., Longerich, H. P. & Strong, D. F. (1990). Determination of the precious metals in geological materials by inductively coupled plasma mass-spectrometry (ICP-MS) with nickel sulphide fire-assay collection and tellurium coprecipitation. *Chemical Geology* **83**, 119–132.

Jenner, F. E., O'Neill, H. S. C., Arculus, R. J. & Mavrogenes, J. A. (2010). The magnetite crisis in the evolution of arc-related magmas and the initial concentrations of Au, Ag, and Cu. *Journal of Petrology* **51**, 2445–2464.

Kane, J. S. (1998). A history of the development and certification of NIST glass SRMs 610–617. *Geostandards Newsletter* **22**, 7–13.

Keays, R. R. & Lightfoot, P. C. (2007). Siderophile and chalcophile metal variations in Tertiary picrites and basalts from West Greenland with implications for the sulphide saturation history of continental flood basalt magmas. *Mineralium Deposita* **42**, 319–336.

Keays, R. R. & Tegner, C. (2015). Magma chamber processes in the formation of the low-sulphide magmatic Au–PGE mineralization of the Platinova Reef in the Skaergaard Intrusion, East Greenland. *Journal of Petrology* (this issue).

Keith, J. D., Whitney, J. A., Hattori, K., Ballantyne, G. H., Christiansen, E. H., Barr, D. L., Cannan, T. M. & Hook, C. J. (1997). The role of magmatic sulfides and mafic alkaline magmas in the Bingham and Tintic mining districts, Utah. *Journal of Petrology* **38**, 1679–1690.

Kouzmanov, K. & Pokrovski, G. S. (2012). Hydrothermal controls on metal distribution in porphyry Cu(-Mo-Au) systems. In: eds. *Special Publication of the Society of Economic Geologists* **16**, 537–618.

Lickfold, V., Cooke, D. R., Crawford, A. J. & Fanning, C. M. (2007). Shoshonitic magmatism and the formation of the Northparkes porphyry Cu–Au deposits, New South Wales. *Australian Journal of Earth Sciences* **54**, 417–444.

Ludwig, K. R. (2012). *User's Manual for Isoplot 3.75: A Geochronological Toolkit for Microsoft Excel. Berkeley Geochronology Center, Special Publication* **5**.

Maksaev, J. V. (1990). Metallogeny, geological evolution, and thermochronology of the Chilean Andes between latitudes 21° and 26° South, and the origin of the major porphyry copper deposits. PhD thesis, Dalhousie University, Halifax, NS, 554 pp.

Maksaev, J. V., Tomlinson, A. J. & Blanco, N. (1994). Estudio geologico de la franja longitudinal comprendida entre Quebrada Blanca y Chuquicamata. Unpublished company report. Servicio Nacional de Geologia y Mineria y Corporación Nacional del Cobre, propuesta para informe final convenio Codelco-Sernageomin, pp. 1–54.

Masterman, G. J., Cooke, D. R., Berry, R. F., Walshe, J. L., Lee, A. W. & Clark, A. H. (2005). Fluid chemistry, structural setting, and emplacement history of the Rosario Cu–Mo porphyry and Cu–Ag–Au epithermal veins, Collahuasi district, northern Chile. *Economic Geology* **100**, 835–862.

McDonough, W. F. & Sun, S.-s. (1995). The composition of the Earth. *Chemical Geology* **120**, 223–253.

Meisel, T. & Moser, J. (2004). Reference materials for geochemical PGE analysis: new analytical data for Ru, Rh, Pd, Os, Ir, Pt and Re by isotope dilution ICP-MS in 11 geological reference materials. *Chemical Geology* **208**, 319–338.

Mudd, G. M., Weng, Z. & Jowitt, S. M. (2013). A detailed assessment of global Cu resource trends and endowments. *Economic Geology* **108**, 1163–1183.

Mungall, J. & Brenan, J. (2014). Partitioning of platinum-group elements and Au between sulfide liquid and basalt and the origins of mantle–crust fractionation of the chalcophile elements. *Geochimica et Cosmochimica Acta* **125**, 265–289.

Munizaga, F., Maksaev, V., Fanning, C. M., Giglio, S., Yaxley, G. & Tassinari, C. C. G. (2008). Late Paleozoic–Early Triassic magmatism on the western margin of Gondwana: Collahuasi area, Northern Chile. *Gondwana Research* **13**, 407–427.

Ossandon, G., Freraut, R., Gustafson, L. B., Lindsay, D. D. & Zentilli, M. (2001). Geology of the Chuquicamata mine: A progress report. *Economic Geology and Bulletin of the Society of Economic Geologists* **96**, 249–270.

Palme, H. & O'Neill, H. S. C. (2014). Cosmochemical estimates of mantle composition. In: Holland, H. D. & Turekian, K. K. (eds) *Treatise on Geochemistry*, 2nd edn. Elsevier, **3**, pp. 1–39.

Park, J. W., Hu, Z., Gao, S., Campbell, I. H. & Gong, H. (2012). Platinum group element abundances in the upper continental crust revisited—New constraints from analyses of Chinese loess. *Geochimica et Cosmochimica Acta* **93**, 63–76.

Park, J.-W., Campbell, I. H. & Arculus, R. J. (2013a). Platinum-alloy and sulfur saturation in an arc-related basalt to rhyolite suite: Evidence from the Pual Ridge lavas, the Eastern Manus Basin. *Geochimica et Cosmochimica Acta* **101**, 76–95.

Park, J. W., Campbell, I. H., Ickert, R. B. & Allen, C. M. (2013b). Chalcophile element geochemistry of the Boggy Plain zoned pluton, southeastern Australia: A S-saturated barren compositionally diverse magmatic system. *Contributions to Mineralogy and Petrology* **165**, 217–236.

Park, J. W., Campbell, I., Kim, J. & Moon, J.-W. (2015). The role of sulfide saturation on formation of a Cu- and Au-rich magma: insights from the platinum group element geochemistry of Niuatahi–Motutahi lavas, Tonga rear arc. *Journal of Petrology* **56**, 59–81.

Peucker-Ehrenbrink, B., Bach, W., Hart, S. R., Blusztajn, J. S. & Abbruzzese, T. (2003). Rhenium–osmium isotope systematics and platinum group element concentrations in oceanic crust from DSDP/ODP Sites 504 and 417/418. *Geochemistry, Geophysics, Geosystems* **4**, 10.1029/2002GC000414.

Plessen, H.-G. & Erzinger, J. (1998). Determination of the Platinum-Group Elements and gold in twenty rock reference materials by inductively coupled plasma-mass spectometry (ICP-MS) after pre-concentration by nickel sulfide fire assay. *Geostandards Newsletter* **22**, 187–194.

Reutter, K. J., Scheuber, E. & Chong, G. (1996). The Precordilleran fault system of Chuquicamata, Northern Chile: Evidence for reversals along arc-parallel strike-slip faults. *Tectonophysics* **259**, 213–228.

Richards, J. P. (2005). Cumulative factors in the generation of giant calc-alkaline porphyry Cu deposits. In: Porter, T. M. (ed.) *Super Porphyry Copper and Gold Deposits: A Global Perspective*. PGC Publishing, pp. 7–25.

Richards, J. P. (2009). Postsubduction porphyry Cu–Au and epithermal Au deposits: Products of remelting of subduction-modified lithosphere. *Geology* **37**, 247–250.

Richards, J. P. (2011*a*). High Sr/Y arc magmas and porphyry Cu ± Mo ± Au deposits: just add water. *Economic Geology* **106**, 1075–1081.

Richards, J. P. (2011*b*). Magmatic to hydrothermal metal fluxes in convergent and collided margins. *Ore Geology Reviews* **40**, 1–26.

Richards, J. P., Boyce, A. J. & Pringle, M. S. (2001). Geologic evolution of the Escondida area, northern Chile: A model for spatial and temporal localization of porphyry Cu mineralization. *Economic Geology and Bulletin of the Society of Economic Geologists* **96**, 271–305.

Ripley, E. M., Brophy, J. G. & Li, C. (2002). Copper solubility in a basaltic melt and sulfide liquid/silicate melt partition coefficients of Cu and Fe. *Geochimica et Cosmochimica Acta* **66**, 2791–2800.

Rohrlach, B. D. (2005). Multi-million year cyclic ramp-up of volatiles in a lower crustal magma reservoir trapped below the Tampakan copper–gold deposit by Mio-Pliocene crustal compression in the Southern Philippines. In: Porter, T. M. (ed.) *Super Porphyry Copper and Gold Deposits: A Global Perspective*. PGC Publishing, pp. 369–407.

Savard, D., Barnes, S.-J. & Meisel, T. (2010). Comparison between nickel–sulfur fire assay Te co-precipitation and isotope dilution with high-pressure asher acid digestion for the determination of platinum-group elements, rhenium and gold. *Geostandards and Geoanalytical Research* **34**, 281–291.

Seedorff, E., Dilles, J. H., Proffett, J. M., Einaudi, M. T., Zurcher, L., Stavast, W. J. A., Johnson, D. A. & Barton, M. C. (2005). Porphyry deposits: characteristics and origin of hypogene features. *Economic Geology, 100th Anniversary Volume* 251–298.

Seedorff, E., Barton, M. D., Stavast, W. J. A. & Maher, D. J. (2008). Root zones of porphyry systems: extending the porphyry model to depth. *Economic Geology* **103**, 939–956.

Sillitoe, R. H. (1997). Characteristics and controls of the largest porphyry copper–gold and epithermal gold deposits in the circum-Pacific region. *Australian Journal of Earth Sciences* **44**, 373–388.

Sillitoe, R. H. (2010). Porphyry copper systems. *Economic Geology* **105**, 3–41.

Tarkian, M. & Stribrny, B. (1999). Platinum-group elements in porphyry copper deposits: a reconnaissance study. *Mineralogy and Petrology* **65**, 161–183.

Tomkins, A. G., Rebryna, K. C., Weinberg, R. F. & Schaefer, B. F. (2012). Magmatic sulfide formation by reduction of oxidized arc basalt. Journal of Petrology **53**, 1537–1567.

Tomlinson, A. J., Maksaev, V. & Blanco, N. (1995). Cuadrangulo Cerro Jaspe. Región de Antofagasta. Map scale, 1:50,000. Servicio Nacional de Geologia y Mineria y Corporación Nacional del Cobre. SERNAGEOMIN Registered report, Santiago, Chile, IR-95-07.

Urqueta, E., Kyser, T. K., Clark, A. H., Stanley, C. R. & Oates, C. J. (2009). Lithogeochemistry of the Collahuasi porphyry Cu–Mo and epithermal Cu–Ag(–Au) cluster, northern Chile: Pearce element ratio vectors to ore. *Geochemistry: Exploration, Environment, Analysis* **9**, 9–17.

Valente, D. L. (2008). The geology, geochemistry and geochronology of the El Abra mine, Chile, and the adjacent Pajonal–El Abra suite of intrusions. Ph.D. thesis, Australian National University, Canberra, 777 pp.

Wilkinson, J. J. (2013). Triggers for the formation of porphyry ore deposits in magmatic arcs. *Nature Geoscience* **6**, 917–925.

Wilson, A. J., Cooke, D. R. & Harper, B. L. (2003). The Ridgeway gold–copper deposit: A high-grade alkalic porphyry deposit in the Lachlan fold belt, New South Wales, Australia. *Economic Geology* **98**, 1637–1666.

Zentilli, M., Krogh, T. E., Maksaev, J. V. & Alpers, C. N. (1994). Uranium–lead dating of zircons from the Chuquicamata and La Escondida porphyry copper deposits, Chile: Inherited zircon cores of Paleozoic age with Tertiary overgrowths. *Comunicaciones*, Universidad de Chile, **45**, 101–110.